

Ab initio quantum many-body description of superconducting trends in the cuprates

Zhi-Hao Cui,^{1,*} Junjie Yang,¹ Johannes Tölle,¹ Hong-Zhou Ye,² Huanchen Zhai,¹ Raehyun Kim,³ Xing Zhang,¹ Lin Lin,^{3,4} Timothy C. Berkelbach,² and Garnet Kin-Lic Chan^{1,†}

¹*Division of Chemistry and Chemical Engineering, California Institute of Technology, Pasadena, California 91125, USA*

²*Department of Chemistry, Columbia University, New York, New York 10027, USA*

³*Department of Mathematics, University of California, Berkeley, California 94720, USA*

⁴*Computational Research Division, Lawrence Berkeley National Laboratory, Berkeley, California 94720, USA*

Using a systematic ab initio quantum many-body approach that goes beyond low-energy models, we directly compute the superconducting pairing order of several doped cuprate materials and structures. We find that we can correctly capture two well-known trends: the pressure effect, where pairing order increases with intra-layer pressure, and the layer effect, where the pairing order varies with the number of copper-oxygen layers. From these calculations, we observe that the strength of superexchange and the covalency at optimal doping are the best descriptors of the maximal pairing order. Our microscopic analysis further identifies short-range copper spin fluctuations, together with multi-orbital charge fluctuations, as central to the pairing trends. Our work illustrates the possibility of a quantitative computational understanding of unconventional high-temperature superconducting materials.

I. INTRODUCTION

Since the discovery of high-temperature superconductivity in the cuprates almost 40 years ago, obtaining a microscopic description of the phenomenon has challenged theoretical material science [1, 2]. In particular, the search for new materials with higher transition temperatures has been hindered by the absence of predictive computational links between the material structure/composition and the observed superconducting temperatures. Here, we describe microscopic calculations that reproduce some of the best-known material trends in cuprate superconducting critical temperatures T_c via the direct ab initio computation of the ground-state pairing order, using only the material structure as input. These rely on new methods to solve the quantum many-body Schrödinger equation in the materials without first simplifying to low-energy models. Analyzing the solutions identifies simple descriptors which correlate with transition temperature and shed light on the nature of the microscopic process of pairing. Overall, our methodology demonstrates the possibility of predictive ab initio computations of high-temperature superconductivity in new materials.

Cuprate superconductors are layered perovskite compounds with two-dimensional copper-oxygen planes separated by buffer layers of atoms, which dope the planes either with electrons or holes. In the parent undoped state, the materials are antiferromagnets, becoming superconducting after doping beyond $\sim 10\%$. Out of the many efforts to increase T_c through altering the composition and structural parameters, some trends can be identified. Two of the clearest ones are the pressure effect and layer effect. In the pressure effect, T_c increases with pressure applied in the plane, rising, e.g. in Hg-1223 from 135 K at ambient pressure to 164 K at 30 GPa [3, 4]. In the layer effect, T_c increases with the number of stacked copper-oxygen planes (e.g. in the mercury-barium cuprates, T_c is 97,

127, 133 K in the 1-, 2-, 3-layer compounds [5]).

Many theories have been proposed to rationalize cuprate superconductivity, but it has proven difficult to obtain a quantitative microscopic picture, and even harder to reproduce the specifics of different cuprate materials. There are two essential complications. First, the phenomenon arises from quantum many-body physics with strong electron interactions, where there are no analytical solutions and no obvious small parameter [6]. (This is in contrast to conventional superconductors with weak electron interactions, where material specific computations are relatively successful [7, 8]). Within any microscopic framework to describe the electron correlation, the predictions thus carry uncertainty from their approximate nature. The second is that the complex material composition complicates the derivation of low-energy Hamiltonians. While one-band Hubbard models and their relatives have informed much current thinking [9, 10], recent accurate numerical solutions of these models have also highlighted the deviation of the model physics from that of the real materials [11–15]. In addition, although there has been limited work to rationalize material specific effects in terms of multi-band models [10, 16–18], the uncertainty introduced into the Hamiltonian arising from downfolding, for instance, due to density functional theory double-counting [19], the definition of impurity orbitals [20], or the difficulties of parametrization or uncertainty of the parametrized form [21], appears comparable to the strength of the material trends. This limits the ability to rationalize T_c in specific materials, such as the layer effect.

In principle, solving the ab initio many-electron Schrödinger equation for the full cuprate material provides an unambiguous and quantitative route to understanding cuprate superconductivity. Although this is traditionally viewed as intractable, recent advances in numerical many-body algorithms and their computational implementation are opening up the possibility of predictive computation even in strongly correlated quantum materials. As one example, we previously captured, and illuminated at the microscopic level, systematic trends in the magnetism of the parent state of the cuprates with such an approach [22]. Here, we show how these strategies may be extended to the much more challenging doped phases of the

* zhcui0408@gmail.com; Present address: Department of Chemistry, Columbia University, New York, New York 10027, USA

† gkc1000@gmail.com

cuprates, and in particular to predict the superconducting pairing order. Below, we describe the advances that now make this work possible, the cuprate systems we will study for their systematic trends, and the results and insights that derive from this approach.

II. QUANTUM SIMULATION METHODS

We aim to approximate, ab initio, the ground-state of the electronic Schrödinger equation of the bulk cuprate (phonon and temperature effects are thus ignored). The strategy has three pieces: a quantum embedding (density matrix embedding theory (DMET)) to connect the bulk many-body problem to a self-consistent impurity many-body problem; the quantum chemical solution of the impurity problem; and the quantum chemical mean-field solution of an auxiliary bulk problem. To retain material specificity, the Hamiltonians use ab initio bare electronic interactions, expressed in a basis of a few hundred of bands, thus no reduced models appear.

Density matrix embedding theory has been introduced elsewhere [23], and its application to doped Hubbard models [11, 24, 25] and ab initio cuprate parent states, extensively benchmarked [22]. We briefly recount essential details in Fig. 1. DMET provides a zero-temperature quantum embedding that maps the interacting bulk problem to the self-consistent solution of two systems: an interacting quantum impurity and an auxiliary mean-field bulk problem. The quantum impurity is taken as a computational supercell (with all atoms) of the material, coupled to a bath constituting the most important orbitals of its environment. The auxiliary bulk Hamiltonian H^{latt} is a mean-field crystal Hamiltonian, augmented by a one-electron operator Δ in each unit cell. The mean-field ground-state Φ^{latt} (a Slater determinant or Bardeen-Cooper-Schrieffer (BCS) state, depending on Δ) determines the bath orbitals, and thus the embedding (impurity plus bath) Hamiltonian $H^{\text{emb}}(\Delta)$. The impurity ground-state Ψ^{emb} then determines the order parameter κ^{emb} . The quantum impurity and auxiliary bulk problems are solved self-consistently with respect to Δ until $\kappa^{\text{latt}}(\Delta) = \kappa^{\text{emb}}(\Delta)$. Δ and κ can acquire finite values for ordered phases due to symmetry breaking in the self-consistency.

In an ab initio description, we start with an atomic orbital representation of the crystal. For bases with reasonable accuracy, this gives rise to many bands, e.g. a few hundred bands per computational cell. The quantum impurity, which contains the orbitals of the atoms in the impurity, thus also contains hundreds of orbitals, and we require an ab initio many-body treatment for such problems. Fortunately, only a few orbitals are strongly correlated, so we can use quantum chemistry strategies designed for this situation: here we primarily use the coupled cluster singles and doubles (CCSD) approximation [26]. Such coupled cluster wavefunctions are widely used in molecular, and more recently materials, modeling and have proved accurate for ordered states (in the current setting we additionally verify their accuracy through other quantum chemical methods, such as the ab initio density matrix renormalization group [27]).

Within the above formulation, the errors can be attributed to three sources: the finite impurity supercell, the finite atomic orbital basis, and approximations in the many-body solver. In principle, these errors can be improved to exactness, as has been analyzed in [22].

In the context of the doped phases of the cuprates, new ingredients appear, such as the treatment of doping. In real materials, doping usually involves dopant atoms, which enlarge the computational cell [28]. For simplicity, we use implicit doping which modifies the charge density while introducing a compensating positive field, either within the “rigid-band” approximation (RBA, uniform background field), or (for a subset of calculations), the virtual crystal approximation [29] (VCA, scaled external field at select atoms). Although detailed results for individual structures are sensitive to the doping formulation, we find trends across the materials to be preserved within a fixed doping scheme.

Another new ingredient is the ab initio simulation of superconducting phases. Defining $\Delta = \sum_{ij} \Delta_{ij} a_i^\dagger a_j^\dagger + \text{H.c.}$ and $\kappa_{ij} = \langle a_j^\dagger a_i^\dagger \rangle$, past a critical doping, the DMET self-consistency produces a finite Δ and κ . Such superconducting solutions are not usually supported by ab initio quantum chemistry solvers. To handle this, we use the Nambu-Gorkov formalism [30] which, for $S_z = 0$ pairing, maps broken particle number symmetry to broken S_z symmetry. This creates a particle-conserving H^{emb} amenable to standard quantum chemistry methods, as further detailed in Sec. 1 of [31].

The scale of the simulations in this work also required additional innovations. For example, to achieve an affordable description of the quantum many-body state, we developed new, compact, Gaussian atomic bases, of correlation-consistent double- ζ plus polarization quality. Similarly, to treat doped states where there is a small band gap, we adapted our orbital localization, self-consistency procedures, and solver algorithms for such near-metallic systems. These and other technical improvements are discussed in Sec. 1 of [31].

The output of the ab initio DMET procedure is a correlated quantum impurity wavefunction Ψ^{emb} and a mean-field bulk wavefunction Φ^{latt} . The former can be used to obtain impurity observables, such as the pairing order, while the latter provides additional information (albeit of limited fidelity) on long-range non-local observables. κ is a multi-orbital quantity, and can be summed into a scalar order parameter with different angular symmetry (in various ways due to the multi-orbital character, see Eqs. (S71) and (S72)); we use m_{SC} to denote the scalar summed quantities, which serve as a proxy for T_c (they are proportional in the BCS theory). The impurity fluctuations that give rise to these orders can be analyzed from Ψ^{emb} .

III. CUPRATE SYSTEMS AND COMPUTATIONS

We consider two series of hole-doped cuprates to study the pressure and layer effects. The first is CCO (CaCuO_2), viewed as a parent compound for a variety of doped cuprates. When mixed with Sr, it has been doped with vacancies (approximate composition $(\text{Ca}_{1-y}\text{Sr}_y)_{1-\delta}\text{CuO}_2$ with $y \sim 0.7$, $\delta \sim 0.1$,

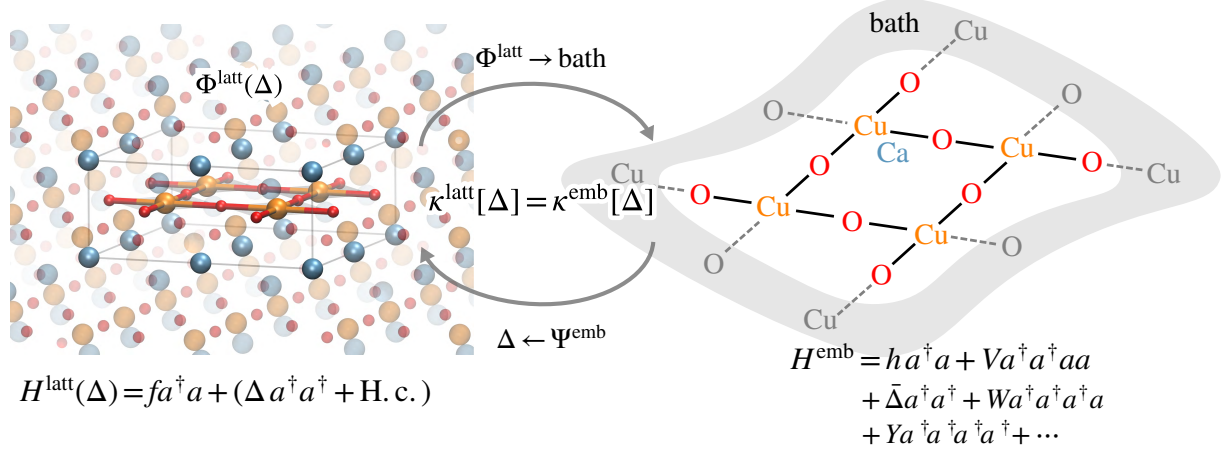


FIG. 1. Computational strategy. The *ab initio* density matrix embedding theory (DMET) framework. This involves solving two ground-state problems: for an auxiliary mean-field Hamiltonian (left), $H^{\text{latt}} = f + \Delta \rightarrow \Phi(\Delta)$, and a quantum impurity + bath Hamiltonian (right), $H^{\text{emb}}(\Delta) \rightarrow \Psi^{\text{emb}}(\Delta)$. Δ is modified by self-consistent iteration until the pairing order κ is the same in the impurity and the auxiliary mean-field problem. The non-number-conserving $\bar{\Delta}$, W , Y terms in H^{emb} arise from the DMET bath construction from $\Phi(\Delta)$. In this work, the bulk problem is represented by 128 cuprate unit cells, and the impurity is a 2×2 supercell, illustrated above for CCO (CaCuO_2).

$T_c \sim 110$ K [32]). The simple structure of parent CCO makes it ideal for studying the pressure effect, while the infinite layer structure provides a natural limiting case for the layer effect. We apply pressure along the a, b axes of the cuprate plane, similar to the experiments in [33], keeping the plane unbuckled.

The second series of compounds are the mercury barium cuprates, single-layer Hg-1201 ($\text{HgBa}_2\text{CuO}_{4+\delta}$) and double-layer Hg-1212 ($\text{HgBa}_2\text{CaCu}_2\text{O}_{6+\delta}$); we consider CCO as the infinite layer parent compound in this series. These compounds are synthesized under conditions with finite oxygen doping. In Hg-1201 we use a structure corresponding to a reported oxygen doping $\delta = 0.19$, associated $T_c \sim 95$ K [34] (additional structures considered in Fig. S9); in Hg-1212, we consider two structures [35]: the oxidized structure (“ox”, with $\delta = 0.22$, $T_c \sim 128$ K), and a variant argon-reduced structure (“red”, close to the undoped compound, $\delta = 0.08$, $T_c \sim 92$ K).

The computations start with a mean-field density functional (DFT) calculation using the Perdew-Burke-Ernzerhof with exact exchange (PBE0) functional in a custom polarized double-zeta Gaussian basis (described in Sec. 2.2 of [31]) using $8 \times 8 \times 2$ \mathbf{k} -points. The increment of doping in the DMET calculation derives from the size of the bulk calculation: we can dope in units of 1/128. Because we do not perform full self-consistency on the charge density (see below) it is necessary to use a mean-field starting point that produces a reasonable charge distribution. We select the PBE0 functional based on its performance relative to accurate quantum many-body embedding benchmarks in our previous work on the parent state [22]. The PBE0 solution is antiferromagnetic (AFM) at half-filling, and in some cases, becomes paramagnetic beyond a certain doping. The PBE0 calculation generates the initial auxiliary mean-field Hamiltonian f (Fig. 1), but this does not enter the many-body impurity Hamiltonian H^{emb} . Thus the correlated DMET calculations do not have a double counting error, but (for finite impurity size) the converged DMET solution retains

some dependence on the initial choice of mean-field f through incomplete relaxation of the charges.

The quantum impurity problem consists of the 2×2 cell of the cuprate and the DMET bath constructed for the valence orbitals in the impurity, yielding a total problem size of 300–900 orbitals. The upper range corresponds to the large cells of the mercury-barium compounds, and to reduce the cost we used coupled sub-impurities to separately treat the CuO_2 and buffer layers [22]; the largest subimpurities contain 376 orbitals. For the results discussed below, we show data from the coupled cluster singles and doubles solver (CCSD) as a compromise between speed and accuracy. Benchmarks in the parent state [22], in the DMET treatment of the 2D one-band Hubbard model and in the *ab initio* cuprate impurity problem (Figs. S3 and S4) suggest we reach sufficient accuracy to discuss the material trends of interest.

To simplify the convergence of the self-consistency, we carry it out with respect to the pairing potential Δ restricted to the three-band $\text{Cu } 3d_{x^2-y^2}$ and $\text{O } 2p_{x(y)}$ orbitals with matrix elements restricted to obey C_{2h} point group symmetry. This allows for the direct update of the pairing density κ (to self-consistency), although it limits self-consistency on the normal charge density itself.

IV. THE PRESSURE EFFECT

We first examine the computed order in CCO at three different in-plane pressures: -15, 0 (ambient), 33 GPa. Without doping, CCO is in an antiferromagnet. At all pressures, under sufficient doping, a superconducting state is formed with predominantly d -wave pairing order, as illustrated by the Cu-Cu pairing order at optimal doping in Fig. 2B; the d -wave character increases with increased pressure. There is also a small s -wave piece in the Cu-Cu pairing, and the total order has a small p -wave component necessarily arising from the

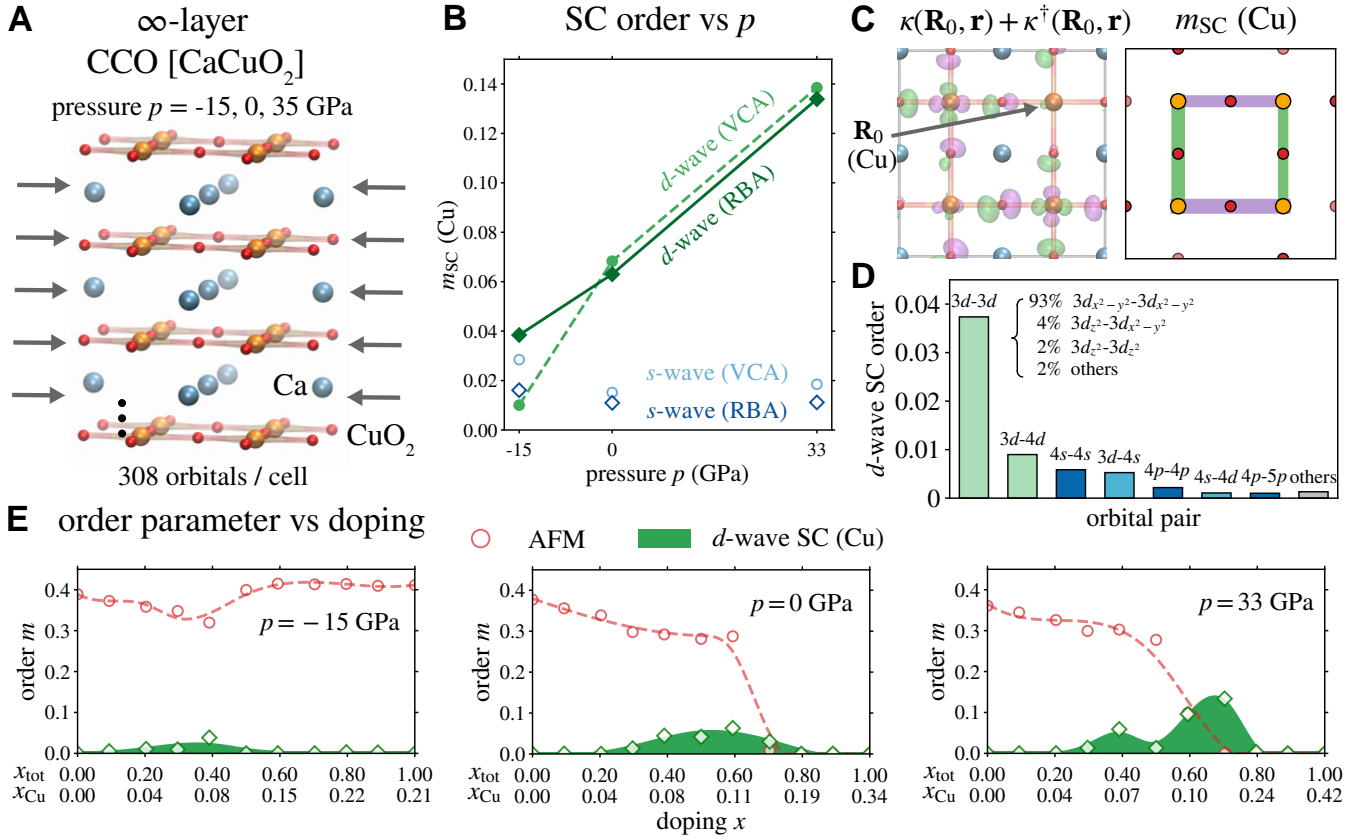


FIG. 2. **Superconducting order and pressure effect.** (A) Structure of the ∞ -layer cuprate CCO (CaCuO_2). (B) d -wave and s -wave order as a function of pressure p , using different doping representations (rigid band approximation (RBA) and virtual crystal approximation (VCA)). (C) Anomalous density $\kappa(\mathbf{R}_0, \mathbf{r}) + \kappa^\dagger(\mathbf{R}_0, \mathbf{r})$ for CCO at optimal doping and ambient pressure. The reference point \mathbf{R}_0 is near the Cu atom in the embedded cell. m_{SC} (Cu): pairing order between neighboring Cu atoms showing d -wave symmetry. (D) Orbital-resolved d -wave SC orders between Cu orbital pairs. (E) AFM and SC order as a function of doping using RBA (VCA curves shown in Fig. S7).

coexistence of AFM and d -wave superconducting order [14]. The uncertainties of the calculation mean that the absolute numerical values for the order should be treated with caution. However, if we use $m_{\text{SC}}^{\text{max}} \propto T_c$ and assume $T_c \sim 100$ K at ambient pressure, then $dT_c/dP \approx 3$ K/GPa, of the same order as that typically seen in experiments (1-2 K/GPa) [36, 37]. Our calculations thus capture a reasonable pressure effect on the maximum superconducting order.

Fig. 2C shows a real-space visualization of the Cu-centered pair amplitude, and the scalar pair amplitude between orbitals on neighboring Cu atoms, for CCO at ambient pressure and optimal doping. The sign of the pairing amplitude illustrates the d -wave symmetry, while the spread (not shown) corresponds to a pair distributed across a linear distance of about 6 unit cells. We show a more detailed orbital resolved analysis of the Cu-Cu d -wave order at optimal doping in Fig. 2D. As illustrated in Fig. S5, as doping increases the pairing orbital character changes, with Cu-Cu pairing at small doping being predominantly $3d$ - $3d$, but at larger dopings containing more $4s$ and $4d$ components. We find that O-O pairing contributes about 30% to the total d -wave order, with Cu-O pairing contributing mainly to the p -wave order.

We now examine in detail the AFM and SC orders as a

function of doping in Fig. 2E. We first discuss the x -axis, the doping axis. When holes are added, the charges go primarily to the CuO_2 plane, and reside mainly on oxygen ($2p$), with a fraction (about 20% - 30%) transferred to Cu; about 90% of the charge resides in the three-band orbitals (Cu $3d_{x^2-y^2}$ and O $2p_{x,y}$). Because the uncompensated moment lies almost entirely on Cu, but the holes reside in hybridized Cu-O orbitals (i.e. the band that is doped does not contain all the uncompensated spin density), the holes do not directly quench the local moment, unlike in the 1-band Hubbard model. Therefore, the decay of the local magnetic order with respect to x_{tot} (number of holes per unit cell) is much slower than in the 1-band Hubbard model, although it is similar to that seen in three-band models for some parameter choices [25]. Our method retains some dependence on the bulk mean-field charge density, so we can obtain unusual behaviour when this charge density is poor. This appears to be the case in the -15 GPa system, where the moment does not decrease even under heavy doping. However, the slow decay of local magnetic order should not be interpreted as a slow decay of global AFM order, as we are missing long-range fluctuations.

In experiments on oxygen doped cuprates, such as yttrium barium copper oxide [38] and the mercury barium cuprates

studied later [39], the effective Cu doping is usually not taken from the estimated oxygen content or x_{tot} (which would naively translate to very large copper oxygen plane dopings), but often inferred from an empirical formula [38, 39]. Thus, it is interesting to analogously replace the bare doping here with the effective Cu doping computed from the atomic populations, x_{Cu} . We then see that the maximum d -wave order appears at dopings (10%-15%) similar to that seen in one-band treatments [40], as well as in the experimental empirical Cu dopings. The optimal doping is close to the point at which the magnetic order suddenly drops. The SC dome contains a double peak structure; this has been seen before in three-band models [25], and appears to be related to the finite size of the impurity cluster.

The quantitative magnetic and pairing orders depend on details of the doping treatment: for example, the difference in the maximum pairing order between a VCA and RBA treatment is shown in Fig. 2B and Fig. S7. This highlights the need to investigate more realistic representations of dopants. However, the qualitative pressure trend in the pairing order is reproduced in either case.

V. THE LAYER EFFECT

We next consider the layer effect in the mercury barium cuprates (1-, 2-layer) and CCO (∞ -layer) compounds. The plot of the maximum pairing order as a function of the layer number is shown in Fig. 3C. We see a sizable increase in the maximum pairing order moving from Hg-1201 to Hg-1212 (ox), similar to the experimental change in T_c . We thus capture the basic experimental trend in T_c of the layer effect. For more than 3 layers, experimentally it is seen that T_c no longer increases, which has been attributed to the potentially inhomogeneous doping of the different copper-oxygen planes. In CCO, inhomogeneous doping is not part of our representation, however, the pairing order decreases slightly from Hg-1212 to CCO, similar to the experimental trend between 3-6 layers, although the small magnitude of the change is challenging within the uncertainty of our numerical approach. Our result for CCO is also in good agreement with the T_c for the mixed Sr/CCO compound (assuming that reflects the T_c of CCO).

The pairing and magnetic orders are shown in Fig. 3D. The qualitative behavior in the mercury-barium cuprates is similar to that in CCO, although here, the hole density is less localized on the Cu atoms, and some fraction goes to buffer atoms (e.g. apical oxygen orbitals). There are other important microscopic differences between the mercury-barium compounds and CCO. For example, in CCO, the magnetic order at half-filling decreases between ambient and 33 GPa pressure, and this is reflected in the more rapid decrease of the local moment close to optimal doping. However, even though the local moment in Hg-1212 decays more slowly than in Hg-1201, the optimal pairing order is larger.

The argon-reduced Hg-1212 structure is similar to the oxygenated structure but has a larger apical Cu-O distance (by about 0.04 Å). Although the experimental sample corresponds to very low oxygen doping where it is not expected to super-

conduct, it is still observed to have a $T_c \sim 92$ K [35], leading to speculation about complex charge-transfer behaviour in mercury barium cuprates. We find that the undoped magnetic behaviour (e.g. exchange couplings and charge distribution) is almost identical in the Hg-1212 (ox) and Hg-1212 (red) structures (see Table S4). Nevertheless, as we dope the reduced structure, we find that holes distribute differently in the reduced and oxidized form, especially near optimal doping ($x_{\text{tot}} \sim 0.5$) where the effective Cu doping is smaller in the reduced structure than the oxidized structure, along with a reduction in pairing order (as in the experiment, but much larger in magnitude). The difference in the Hg-1212 (ox) and Hg-1212 (red) electron densities is shown in Fig. 3E: the main difference corresponds to a transfer of charge from the in-plane O 2p orbitals in the (red) structure, to the apical O and Hg orbitals in the (ox) structure, leaving the Hg-1212 (ox) with a larger in-plane doping. The sensitivity of pairing order to the charge distribution highlights the need to further investigate the treatment of doping and the charge density. Overall, the complicated behaviour confirms the importance of atomic scale crystal structure in the development of the pairing order in these multicomponent, multilayer cuprates (see also Sec. 3.5 of [31]).

VI. DESCRIPTORS FOR SUPERCONDUCTIVITY IN THE CUPRATES

Our ab initio calculations above capture the correct pressure and layer effects on pairing order across several cuprate structures and compositions. We can therefore interrogate these in silico solutions to identify the features of the electronic structure that most correlate with these trends.

In Fig. 4 we plot maximum pairing order against a variety of descriptors: (i) the magnetic (nearest neighbour Heisenberg) exchange parameter J , derived from the same ab initio methodology applied at half-filling following [22], (ii) oxygen hole content at optimal doping (Δn_O), (iii) the bond order between Cu 3d-O 2p ($\sim \langle a_{3d_{x^2-y^2}}^\dagger a_{2p_{x(y)}} \rangle$, see Eq. (S68)). (i) and (ii) have previously been invoked as descriptors in the literature (see e.g. [41]); exchange has been associated with cuprate superconductivity since the earliest discussions [42, 43] and its correlation with T_c has attracted much experimental interest [41, 44]. Both (ii) and (iii) are related to the charge-transfer gap and covalency of the Cu-O bond, which are commonly discussed in theoretical treatments [18, 45] as well as in various experiments [44, 46]. However, it should be noted that (ii) and (iii) are related but different probes of these quantities: (ii) measures the diagonal part of the density matrix, while (iii) measures the off-diagonal part.

We see pairing order correlates quite well with the exchange parameter J , capturing both the pressure and layer effect. We note that the systematics of the layer effect are subtle, and involve both mean-field [47] and correlated electronic effects [22] with the apical orbitals. However, there are important outliers: for example, it obtains the wrong ordering for Hg-1212 (red) and Hg-1212 (ox), which have almost the same J but very different pairing orders. This is unsurprising,

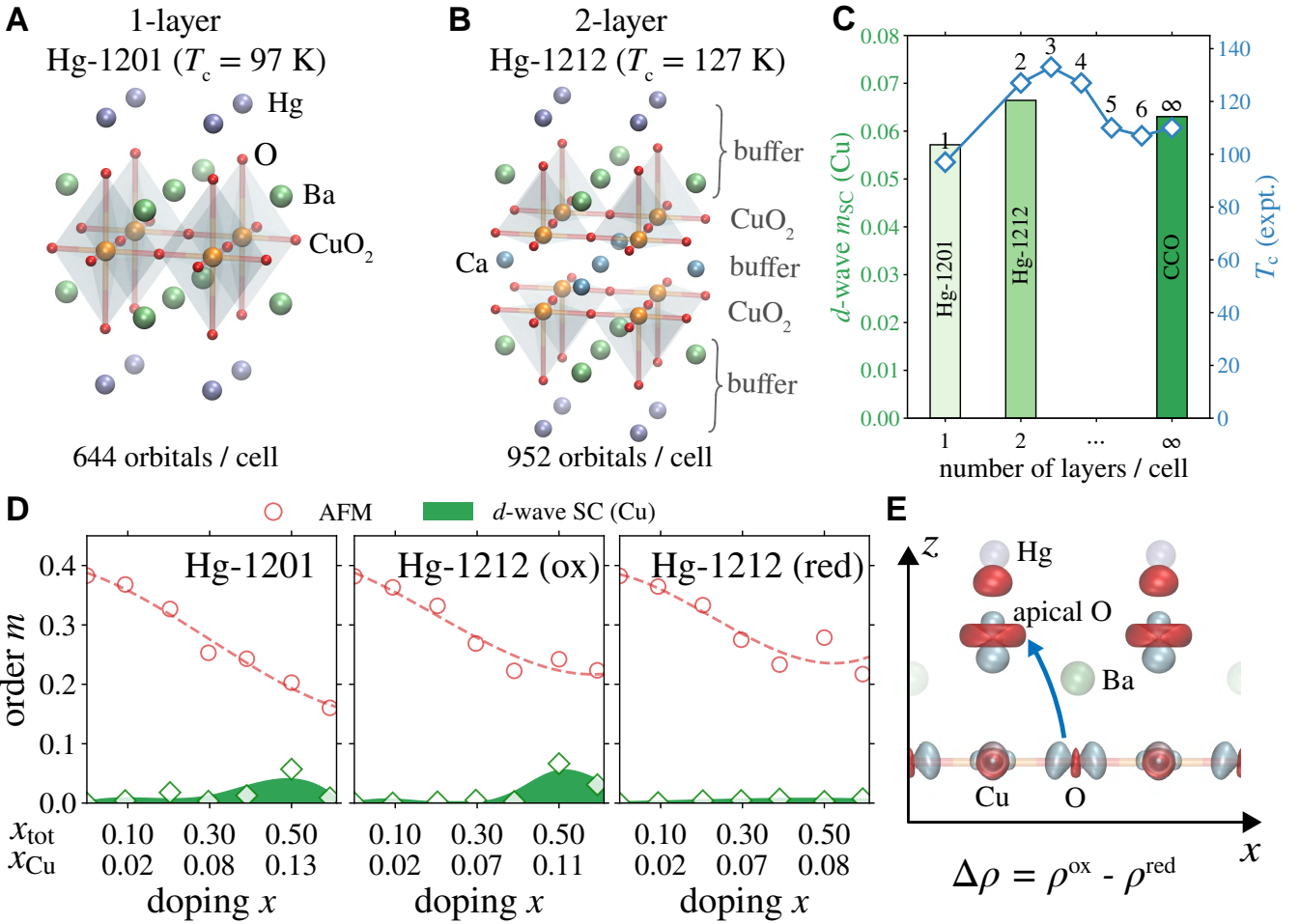


FIG. 3. **Layer effect.** Structures of (A) single-layer Hg-1201 ($\text{HgBa}_2\text{CuO}_4$) and (B) double-layer Hg-1212 ($\text{HgBa}_2\text{CaCu}_2\text{O}_6$); (C) Comparison between calculated d -wave SC orders (Hg-1201, Hg-1212, and CCO) and experimental T_c (data from [5, 32]) as a function of the number of layers per cell. (D) AFM and SC orders of different compound structures (Hg-1201, oxidized Hg-1212, and reduced Hg-1212). (E) Electron density difference between oxidized and reduced Hg-1212 at optimal doping (red: increased electron density of oxidized vs. reduced, blue: decreased electron density). Arrow indicates the transfer of charge between reduced and oxidized structures.

because J is derived from magnetism in the undoped compound, and neglects material specific aspects of doping. We emphasize also that the correlation between J and pairing order appears in our study in a material-specific manner, where both quantities are obtained within the same computational approximation.

Unlike J , oxygen hole content at optimal doping is a descriptor in the doped state. It also correlates with the pairing order (capturing the pressure effect) and for example, successfully distinguishes between Hg-1212 (red) and Hg-1212 (ox), unlike J . However, it places Hg-1201 and Hg-1212 (ox) in the wrong order, and thus does not capture the layer effect. Similarly, the bond-order at optimal doping measures the effective Cu-O hopping matrix element that enters into the super-exchange process, but is evaluated with the effects of doping. The bond-order is overall the best descriptor in terms of the linear fit, but similar to the oxygen hole content, does not capture the layer effect between Hg-1201 and Hg-1212 (ox) (although it does better than the oxygen hole content descriptor).

The correlations between the above local descriptors, the computed pairing order, and the experimental pressure and layer effects, indicate that the processes driving these systematics in pairing can be understood in terms of the quantum correlations at a relatively local level, which we now analyze.

VII. MICROSCOPIC ANALYSIS OF FLUCTUATIONS AND PAIRING

To obtain a clearer understanding of the microscopic processes driving pairing, we now try to identify the most important fluctuations in the correlated quantum impurity wavefunctions Ψ^{emb} . Within the coupled cluster singles and doubles solver, $\Psi^{\text{emb}} = e^{T_1+T_2} |\text{m.f.}\rangle$, where $|\text{m.f.}\rangle$ is a Slater determinant (in the non-SC phase) and a BCS state (in the doped SC phase), where the mean-field is determined by the DMET self-consistency. T_1 is an operator containing quadratic fermion terms ($a^\dagger a$, $a^\dagger a^\dagger$), while T_2 contains quartic fermion terms

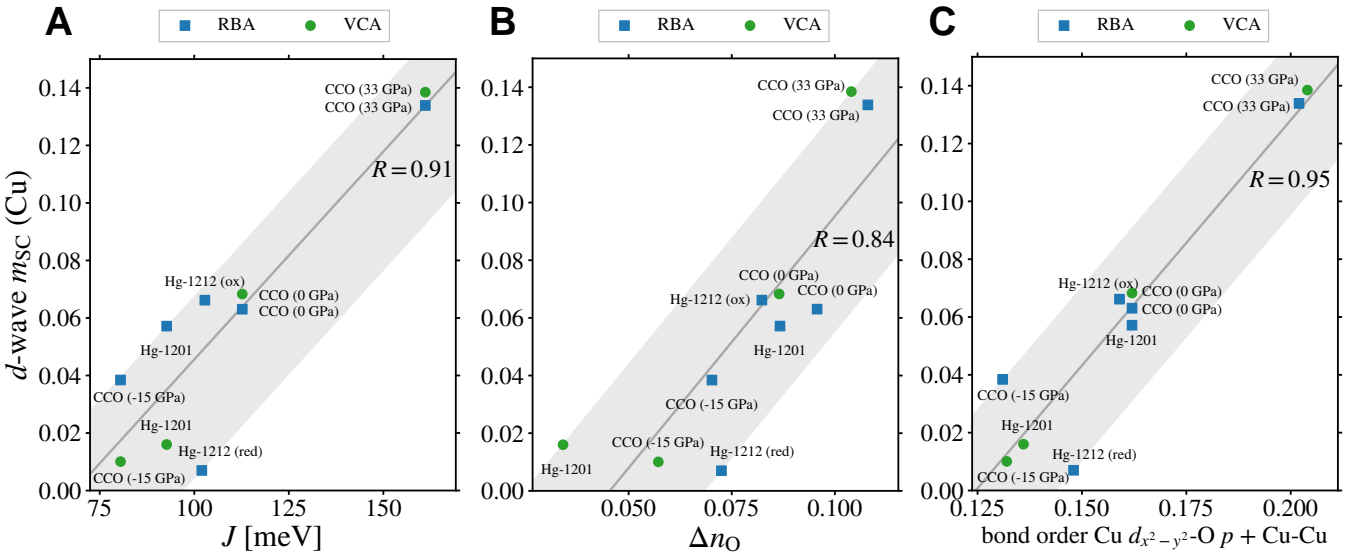


FIG. 4. Descriptors of superconductivity. Correlation between superconducting order and selected descriptors: (A) Super-exchange coupling parameter J at half-filling. (B) Average number of holes on oxygen Δn_O at optimal doping. (C) Bond order (off-diagonal measure of covalency) at optimal doping. Linear regression R values are also shown. RBA, VCA: rigid band approximation, virtual crystal approximation.

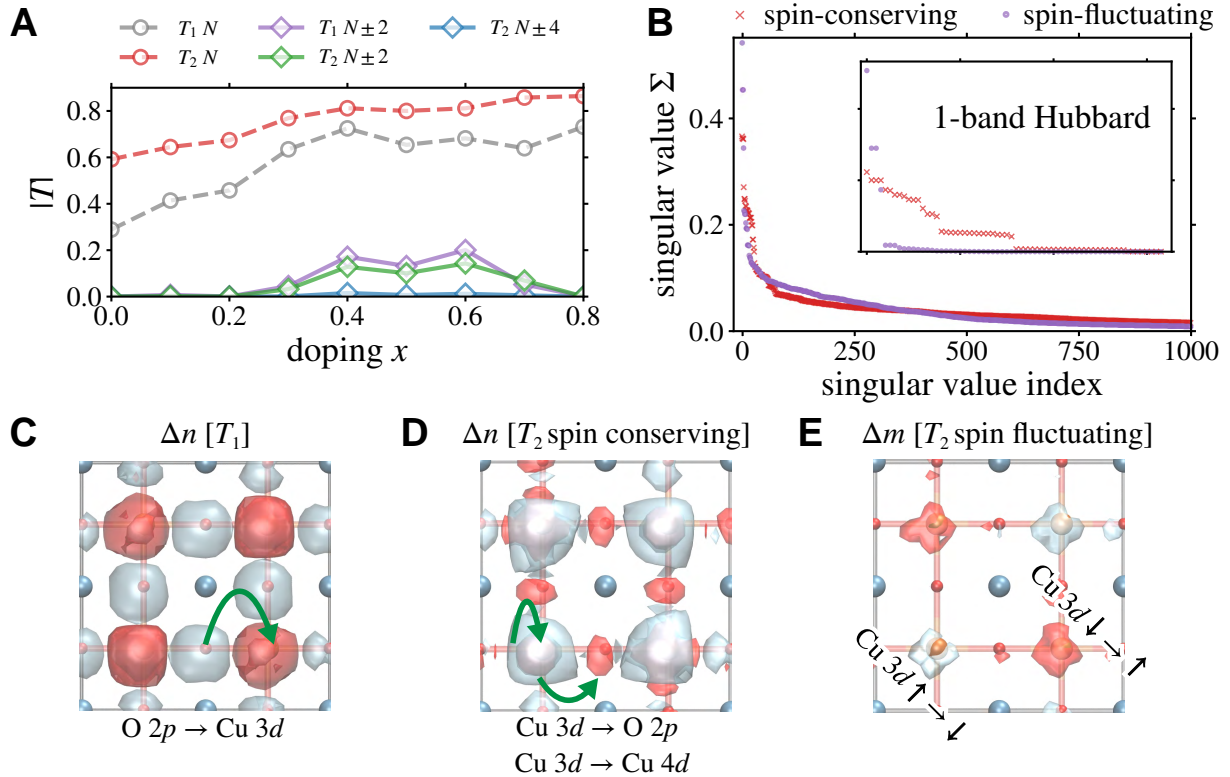


FIG. 5. Microscopic analysis. (A) Norm of different blocks of coupled-cluster amplitudes (N : normal fluctuations, $N \pm 2$, $N \pm 4$ anomalous fluctuations). (B) Singular values of different T_2 decompositions [spin conserving ($\Delta S_z = 0$) or spin fluctuating ($\Delta S_z = \pm 1$)] in an ab initio cuprate calculation (CCO, ambient pressure); inset: T_2 decomposition in the one-band Hubbard model plaquette DMET at $U = 6$. (C) Effect of largest singular mode of T_1 on the charge density n (red: density increase; blue: density decrease): charge shifts from oxygen to copper. (D) Effect of the largest singular mode of T_2 (spin-conserving decomposition) on the charge density: charge shifts from $\text{Cu } 3d$ to empty Cu orbitals (breathing) and to O. (E) Effect of the largest left, right singular modes of T_2 (spin-fluctuating decomposition) on the spin density: the moments along the diagonal increase (red)/decrease (blue).

$(a^\dagger a^\dagger a a, a^\dagger a^\dagger a^\dagger a, a^\dagger a^\dagger a^\dagger a^\dagger, \dots)$; the exponentiation allows T_1 to capture disconnected fluctuations of individual particles,

while T_2 describes the connected fluctuations of pairs of particles. We can further classify T_1 and T_2 into components that produce different changes in the particle number: N (normal fluctuations which do not change particle number), and $N \pm 2, \pm 4$ (anomalous fluctuations). In Fig. 5A, we show the magnitude of the components of T_1 and T_2 after DMET self-consistency. We see that the total fluctuations increase as the system is doped, and at intermediate dopings, because of particle number symmetry breaking, there are anomalous fluctuations. The main anomalous fluctuations modify the pairing order directly ($T_1 N \pm 2$) or modify the pairing while coupled to a particle-hole excitation ($T_2 N \pm 2$). Nonetheless, even in the superconducting state, the anomalous fluctuations are much smaller than the normal fluctuations.

The effect of the T_1 fluctuation on the charge density is visualized in Fig. 5C. The primary components of T_1 are excitations between O $2p$ and Cu $3d$ orbitals, resulting in a shift of charge density from oxygen to copper. The effect of this correlation-stabilized fluctuation (i.e. it appears only in the presence of non-zero T_2) is to make the copper-oxygen bond more covalent than expected in a simple mean-field treatment.

The four-fermion T_2 amplitude can be decomposed into quadratic fluctuations through a principal component analysis, similar to decompositions of the four-fermion (two-particle) Green's functions [48]. We write $T_2 = \sum_m w_m O_m^\dagger O_m$, and then large weights w_m denote dominant fluctuations. Indeed, within a random phase approximation, the O_m are bosonic operators, and if there is a dominant bosonic mode that is driving the superconducting instability, we would expect this to appear as a large singular value w_m . Because T_2 preserves S_z symmetry, we can carry out the decomposition into two channels: $\{O_m\}$ such that $[O_m, S_z] = 0$ (spin-conserving channel), or $[O_m, S_z] = \pm 1$ (spin-fluctuation channel).

Fig. 5B shows the ordered singular values in the spin-conserving and spin-fluctuating channels for CCO at ambient pressure. (For comparison we show the same analysis for the DMET plaquette treatment of the 2D pure one-band Hubbard model at $U = 6$). We see that the largest singular values in the spin-fluctuating channel are larger than in the spin-conserving channel; the spin fluctuations are therefore more dominant. There are some similarities between the modes in the CCO materials and in the one-band Hubbard model, in particular, we see 4 large singular values in the $S_z \pm 1$ channel in both cases (corresponding to the fluctuations that reduce local spin polarization). However, the distribution is less peaked in the ab initio case, and the difference between the spin-conserving and spin-fluctuating channels is less pronounced. We visualize the dominant modes in Figs. 5D, E. In the spin-conserving channel, the first 4 fluctuations mainly involve charge redistribution from Cu $3d$ to other orbitals, principally, the oxygen $2p$ orbitals and Cu $4d$ (details in Table S5). These types of multi-orbital charge fluctuations, i.e. involving modes such as “breathing mode” $3d \rightarrow 4d$ excitations [49] and buffer layer excitations beyond the three-band in-plane orbitals of the cuprates, have previously been shown to be essential to capturing material-specific trends in the magnetism in the layer effect [22]. In the spin-fluctuating channel, the first 4 fluctuations primarily flip the spin densities in the Cu

$3d_{x^2-y^2}$ orbitals. Combined with the importance of the superexchange descriptor in predicting the pairing order trends, the microscopic analysis suggests that the main fluctuations driving the trends are short-range spin fluctuations. However, in our fully ab initio microscopic picture, additional large fluctuations (such as breathing modes and charge redistribution) associated with covalency are required, as they generate the energy scale of superexchange. This is an essential difference with low-energy 1-band representations.

VIII. CONCLUSIONS

In this work, we have demonstrated a fully ab initio many-body simulation strategy that, starting from the material structure, directly approximates the solution of the electronic Schrödinger equation to obtain the superconducting pairing order across a range of geometries and compositions of cuprate materials. We note what is not yet contained within our current treatment: there are no phonons, or long-range spin or charge fluctuations (at distances much larger than the computational cell), the treatment of doping does not include explicit dopants and the associated structural relaxation and disorder, nor are the solvers and representations numerically exact (for a detailed analysis of outstanding limitations, see Sec. 4 of [31]). Consequently, there remain important differences between the results of the simulations and observations in real materials. Nonetheless, we are able to reproduce two of the known systematic trends in the cuprate materials: the increase in maximum pairing order as a function of intralayer pressure; and the increase (and decrease) in maximum pairing order as a function of the number of stacked copper-oxygen layers. That these trends correctly appear indicates that the physics and numerical aspects of the calculation likely contain important and relevant ingredients to describe superconducting pairing in a quantitative manner across a range of cuprate materials.

Detailed analysis of our calculations confirms some long-standing proposals for the driving force for pairing in cuprates, but also provides new insights. Superexchange, suitably defined, correlates well with maximum pairing order, and short-range spin fluctuations, mainly on the copper atoms, drive the pairing. However, the ab initio picture of the fluctuations is richer than that in simplified models, because multi-orbital effects associated with covalency are needed to facilitate the spin fluctuations. Such multi-orbital processes are key to material-specific trends.

The current work shows that a material-specific understanding of superconductivity in the cuprates is now conceivable through direct computation. This is a step towards enabling a material driven understanding of the full phase diagram, the elucidation of the microscopic mechanisms underlying the phases, and the computational search for new high-temperature superconducting materials.

ACKNOWLEDGMENTS

Funding: This work was primarily supported by the US Department of Energy, Office of Science, via grant no. DE-SC0018140. G.K.-L.C. is a Simons Investigator in Physics. Calculations were performed using the facilities of National Energy Research Scientific Computing Center (NERSC), a U.S. Department of Energy Office of Science User Facility located at Lawrence Berkeley National Laboratory, under NERSC award ERCAP0023924, and in the Resnick High Performance Computing Center, supported by the Resnick Sustainability Institute at Caltech. We thank M. Graf and C. Mewes for arranging for computational time on NERSC. This work was partially supported by the National Science

Foundation under Award No. CHE-1848369 (H.-Z.Y.) and the Air Force Office of Scientific Research under Award No. FA9550-18-1-0095 (R. K.). L. L. is a Simons Investigator. J.T. acknowledges funding by the Deutsche Forschungsgemeinschaft (DFG, German Research Foundation) through DFG-495279997.

Data and codes used in this work are in the supplementary materials or the repositories below or can be obtained from the authors upon reasonable request. The LIBD-MET repository is at github.com/gkclab/libdmet_preview. The BLOCK2 code repository is at github.com/block-hczhai/block2-preview. PySCF is available from pyscf.org.

Supplementary materials: Methods, Figures S1-S9, Tables S1-S5, References.

[1] N. Plakida, *High-temperature cuprate superconductors: Experiment, theory, and applications*, Vol. 166 (Springer Science & Business Media, 2010).

[2] M. R. Norman, The challenge of unconventional superconductivity, *Science* **332**, 196 (2011).

[3] L. Gao, Y. Xue, F. Chen, Q. Xiong, R. Meng, D. Ramirez, C. Chu, J. Eggert, and H. Mao, Superconductivity up to 164 K in $HgBa_2Ca_{m-1}Cu_mO_{2m+2+\delta}$ ($m = 1, 2$, and 3) under quasihydrostatic pressures, *Phys. Rev. B* **50**, 4260 (1994).

[4] A. Yamamoto, N. Takeshita, C. Terakura, and Y. Tokura, High pressure effects revisited for the cuprate superconductor family with highest critical temperature, *Nat. comm.* **6**, 8990 (2015).

[5] E. Antipov, A. Abakumov, and S. Putilin, Chemistry and structure of Hg-based superconducting Cu mixed oxides, *Supercond. Sci. Tech.* **15**, R31 (2002).

[6] E. Dagotto, Complexity in strongly correlated electronic systems, *Science* **309**, 257 (2005).

[7] L. N. d. Oliveira, E. Gross, and W. Kohn, Density-functional theory for superconductors, *Phys. Rev. Lett.* **60**, 2430 (1988).

[8] M. Lüders, M. Marques, N. Lathiotakis, A. Floris, G. Profeta, L. Fast, A. Continenza, S. Massidda, and E. Gross, Ab initio theory of superconductivity. I. Density functional formalism and approximate functionals, *Phys. Rev. B* **72**, 024545 (2005).

[9] M. Qin, T. Schäfer, S. Andergassen, P. Corboz, and E. Gull, The Hubbard model: A computational perspective, *Annu. Rev. Condens. Matter Phys.* **13**, 275 (2022).

[10] M. T. Schmid, J.-B. Morée, Y. Yamaji, and M. Imada, Superconductivity studied by solving ab initio low-energy effective Hamiltonians for carrier doped $CaCuO_2$, $Bi_2Sr_2CuO_6$, $Bi_2Sr_2CaCu_2O_8$, and $HgBa_2CuO_4$, arXiv preprint arXiv:2303.06672 (2023).

[11] B.-X. Zheng, C.-M. Chung, P. Corboz, G. Ehlers, M.-P. Qin, R. M. Noack, H. Shi, S. R. White, S. Zhang, and G. K.-L. Chan, Stripe order in the underdoped region of the two-dimensional Hubbard model, *Science* **358**, 1155 (2017).

[12] E. W. Huang, C. B. Mendl, S. Liu, S. Johnston, H.-C. Jiang, B. Moritz, and T. P. Devereaux, Numerical evidence of fluctuating stripes in the normal state of high- T_c cuprate superconductors, *Science* **358**, 1161 (2017).

[13] M. Qin, C.-M. Chung, H. Shi, E. Vitali, C. Hubig, U. Schollwöck, S. R. White, and S. Zhang, Absence of superconductivity in the pure two-dimensional Hubbard model, *Phys. Rev. X* **10**, 031016 (2020).

[14] S. Jiang, D. J. Scalapino, and S. R. White, Ground-state phase diagram of the $t-t'-J$ model, *Proc. Natl. Acad. Sci.* **118**, e2109978118 (2021).

[15] P. Mai, N. S. Nichols, S. Karakuzu, F. Bao, A. Del Maestro, T. A. Maier, and S. Johnston, Robust charge-density-wave correlations in the electron-doped single-band Hubbard model, *Nat. Comm.* **14**, 2889 (2023).

[16] P. R. C. Kent, T. Saha-Dasgupta, O. Jepsen, O. K. Andersen, A. Macridin, T. A. Maier, M. Jarrell, and T. C. Schulthess, Combined density functional and dynamical cluster quantum Monte Carlo calculations of the three-band Hubbard model for hole-doped cuprate superconductors, *Phys. Rev. B* **78**, 035132 (2008).

[17] C. Weber, C. Yee, K. Haule, and G. Kotliar, Scaling of the transition temperature of hole-doped cuprate superconductors with the charge-transfer energy, *EPL* **100**, 37001 (2012).

[18] N. Kowalski, S. S. Dash, P. Sémond, D. Sénéchal, and A.-M. Tremblay, Oxygen hole content, charge-transfer gap, covalency, and cuprate superconductivity, *Proc. Natl. Acad. Sci.* **118**, e2106476118 (2021).

[19] X. Wang, L. De'Medici, H. Park, C. Marianetti, and A. J. Millis, Covalency, double-counting, and the metal-insulator phase diagram in transition metal oxides, *Phys. Rev. B* **86**, 195136 (2012).

[20] J. Karp, A. Hampel, and A. J. Millis, Dependence of DFT+DMFT results on the construction of the correlated orbitals, *Phys. Rev. B* **103**, 195101 (2021).

[21] S. Jiang, D. J. Scalapino, and S. R. White, A single-band model with enhanced pairing from dmrg-based downfolding of the three-band hubbard model, arXiv preprint arXiv:2303.00756 (2023).

[22] Z.-H. Cui, H. Zhai, X. Zhang, and G. K.-L. Chan, Systematic electronic structure in the cuprate parent state from quantum many-body simulations, *Science* **377**, 1192 (2022).

[23] G. Knizia and G. K.-L. Chan, Density matrix embedding: A simple alternative to dynamical mean-field theory, *Phys. Rev. Lett.* **109**, 186404 (2012).

[24] J. P. F. LeBlanc, A. E. Antipov, F. Becca, I. W. Bulik, G. K.-L. Chan, C.-M. Chung, Y. Deng, M. Ferrero, T. M. Henderson, C. A. Jiménez-Hoyos, E. Kozik, X.-W. Liu, A. J. Millis, N. V. Prokof'ev, M. Qin, G. E. Scuseria, H. Shi, B. V. Svistunov, L. F. Tocchio, I. S. Tupitsyn, S. R. White, S. Zhang, B.-X. Zheng, Z. Zhu, and E. Gull, Solutions of the two-dimensional Hubbard

model: Benchmarks and results from a wide range of numerical algorithms, *Phys. Rev. X* **5**, 041041 (2015).

[25] Z.-H. Cui, C. Sun, U. Ray, B.-X. Zheng, Q. Sun, and G. K.-L. Chan, Ground-state phase diagram of the three-band Hubbard model from density matrix embedding theory, *Phys. Rev. Research* **2**, 043259 (2020).

[26] I. Shavitt and R. J. Bartlett, *Many-Body methods in chemistry and physics: MBPT and coupled cluster Theory* (Cambridge University, 2009).

[27] G. K.-L. Chan and S. Sharma, The density matrix renormalization group in quantum chemistry, *Ann. Rev. Phys. Chem.* **62**, 465 (2011).

[28] J. W. Furness, Y. Zhang, C. Lane, I. G. Buda, B. Barbiellini, R. S. Markiewicz, A. Bansil, and J. Sun, An accurate first-principles treatment of doping-dependent electronic structure of high-temperature cuprate superconductors, *Comm. Phys.* **1**, 1 (2018).

[29] L. Bellaiche and D. Vanderbilt, Virtual crystal approximation revisited: Application to dielectric and piezoelectric properties of perovskites, *Phys. Rev. B* **61**, 7877 (2000).

[30] Y. Nambu, Quasi-particles and gauge invariance in the theory of superconductivity, *Phys. Rev.* **117**, 648 (1960).

[31] See supplementary materials.

[32] M. Azuma, Z. Hiroi, M. Takano, Y. Bando, and Y. Takeda, Superconductivity at 110 K in the infinite-layer compound $(\text{Sr}_{1-x}\text{Ca}_x)_{1-y}\text{CuO}_2$, *Nature* **356**, 775 (1992).

[33] F. Hardy, N. Hillier, C. Meingast, D. Colson, Y. Li, N. Barišić, G. Yu, X. Zhao, M. Greven, and J. Schilling, Enhancement of the critical temperature of $\text{HgBa}_2\text{CuO}_{4+\delta}$ by applying uniaxial and hydrostatic pressure: implications for a universal trend in cuprate superconductors, *Phys. Rev. Lett.* **105**, 167002 (2010).

[34] Q. Huang, J. Lynn, Q. Xiong, and C. Chu, Oxygen dependence of the crystal structure of $\text{HgBa}_2\text{CuO}_{4+\delta}$ and its relation to superconductivity, *Phys. Rev. B* **52**, 462 (1995).

[35] P. Radaelli, J. Wagner, B. Hunter, M. Beno, G. Knapp, J. Jorgensen, and D. Hinks, Structure, doping and superconductivity in $\text{HgBa}_2\text{CaCu}_2\text{O}_{6+\delta}$ ($T_c \leq 128$ K), *Physica C: Supercond.* **216**, 29 (1993).

[36] B. Lorenz and C. Chu, High pressure effects on superconductivity (Springer, 2005) pp. 459–497.

[37] J. S. Schilling, High-pressure effects, *Handbook of High-temperature Superconductivity: Theory and Experiment*, 427 (2007).

[38] R. Liang, D. Bonn, and W. Hardy, Evaluation of cu_2 plane hole doping in $\text{YBa}_2\text{Cu}_3\text{O}_{6+x}$ single crystals, *Phys. Rev. B* **73**, 180505 (2006).

[39] A. Yamamoto, W.-Z. Hu, and S. Tajima, Thermoelectric power and resistivity of $\text{HgBa}_2\text{CuO}_{4+\delta}$ over a wide doping range, *Phys. Rev. B* **63**, 024504 (2000).

[40] B.-X. Zheng and G. K.-L. Chan, Ground-state phase diagram of the square lattice Hubbard model from density matrix embedding theory, *Phys. Rev. B* **93**, 035126 (2016).

[41] L. Wang, G. He, Z. Yang, M. Garcia-Fernandez, A. Nag, K. Zhou, M. Minola, M. L. Tacon, B. Keimer, Y. Peng, and Y. Li, Paramagnons and high-temperature superconductivity in a model family of cuprates, *Nat. Comm.* **13**, 3163 (2022).

[42] P. W. Anderson, The resonating valence bond state in La_2CuO_4 and superconductivity, *Science* **235**, 1196 (1987).

[43] F. C. Zhang and T. M. Rice, Effective Hamiltonian for the superconducting Cu oxides, *Phys. Rev. B* **37**, 3759 (1988).

[44] S. M. O'Mahony, W. Ren, W. Chen, Y. X. Chong, X. Liu, H. Eisaki, S.-i. Uchida, M. Hamidian, and J. S. Davis, On the electron pairing mechanism of copper-oxide high temperature superconductivity, *Proc. Natl. Acad. Sci.* **119**, e2207449119 (2022).

[45] C. Weber, K. Haule, and G. Kotliar, Strength of correlations in electron-and hole-doped cuprates, *Nat. Phys.* **6**, 574 (2010).

[46] M. Jurkutat, C. Kattinger, S. Tsankov, R. Reznicek, A. Erb, and J. Haase, How pressure enhances the critical temperature of superconductivity in $\text{YBa}_2\text{Cu}_3\text{O}_{6+y}$, *Proc. Natl. Acad. Sci.* **120**, e2215458120 (2023).

[47] E. Pavarini, I. Dasgupta, T. Saha-Dasgupta, O. Jepsen, and O. Andersen, Band-structure trend in hole-doped cuprates and correlation with $T_{\text{c max}}$, *Phys. Rev. Lett.* **87**, 047003 (2001).

[48] X. Dong, L. Del Re, A. Toschi, and E. Gull, Mechanism of superconductivity in the hubbard model at intermediate interaction strength, *Proc. Natl. Acad. Sci.* **119**, e2205048119 (2022).

[49] N. A. Bogdanov, G. Li Manni, S. Sharma, O. Gunnarsson, and A. Alavi, Enhancement of superexchange due to synergetic breathing and hopping in corner-sharing cuprates, *Nat. Phys.* **18**, 190 (2022).

Supplementary Materials for “Ab initio quantum many-body description of superconducting trends in the cuprates”

Zhi-Hao Cui ^{1†§}, Junjie Yang ¹, Johannes Tölle ¹,
Hong-Zhou Ye ², Huachen Zhai ¹, Raehyun Kim ³, Xing Zhang ¹,
Lin Lin ^{3,4}, Timothy C. Berkelbach ², Garnet Kin-Lic Chan ^{1*}

¹Division of Chemistry and Chemical Engineering, California Institute of Technology,
Pasadena, California 91125, USA

²Department of Chemistry, Columbia University, New York, New York 10027, USA

³Department of Mathematics, University of California, Berkeley, California 94720, USA

⁴Computational Research Division, Lawrence Berkeley National Laboratory,
Berkeley, California 94720, USA

†E-mail: zhcui0408@gmail.com. *E-mail: gkc1000@gmail.com.

Contents

1 Methods	2
1.1 Quantum chemistry formalism for superconductivity	2
1.1.1 Recap of BCS theory, the Nambu representation, and pairing symmetry	2
1.1.2 Ab initio superconducting Hamiltonians	4
1.1.3 DMET algorithms for superconducting states	8
1.2 Localized orbitals for metallic systems	9
1.3 Ab initio many-body impurity solver	10
1.4 Correlation potential matching between lattice and embedded impurity	12
1.5 Analysis methods	13
2 Computational details	16
2.1 Atomic modelling of doping	16
2.2 Optimization of Gaussian basis sets	17
2.3 Mean-field settings	18
2.4 DMET settings	19
3 Additional data	19
3.1 Ab initio impurity solver benchmarks and order parameters	19
3.2 Virtual crystal approximation data	22
3.3 Influence of lattice smearing temperature	22
3.4 Comparison between reduced and oxidized structures of Hg-1212	23
3.5 Effect of geometry in Hg-1201	23
3.6 Coupled-cluster amplitude decomposition data	24
4 Limitations of the current work	25
5 Reference	26

[§]Present address: Department of Chemistry, Columbia University, New York, New York 10027, USA.

1 Methods

In the sections below, we describe specifics of the DMET formalism, quantum chemistry solvers, and analysis as used in the main text. In the first two cases, we focus only on those aspects new to ab initio DMET applications to superconducting ground-states; we do not recount the entire ab initio DMET quantum chemistry technology. The ab initio DMET implementation is described in detail in Ref. [50] and the SI of Ref. [22].

1.1 Quantum chemistry formalism for superconductivity

1.1.1 Recap of BCS theory, the Nambu representation, and pairing symmetry

Bardeen–Cooper–Schrieffer (BCS) theory provides a mean-field treatment of superconductivity. In this theory, superconducting order corresponds to a non-zero expectation value of $\langle a^\dagger a^\dagger \rangle$ and $\langle aa \rangle$. In other words, particle number is not conserved in the BCS ground-state, and superconductivity corresponds to a broken particle-number symmetry ($U(1)$ symmetry).

The original BCS formulation uses a one-band picture and a simplified two-electron Hamiltonian,

$$\hat{H}^{\text{simplified}} = \sum_{\mathbf{k}\sigma} (\varepsilon_{\mathbf{k}} - \mu) a_{\mathbf{k}\sigma}^\dagger a_{\mathbf{k}\sigma} - \sum_{\mathbf{k}\mathbf{k}'} V_{\mathbf{k}\mathbf{k}'} a_{\mathbf{k}\alpha}^\dagger a_{-\mathbf{k}\beta}^\dagger a_{-\mathbf{k}'\beta} a_{\mathbf{k}'\alpha}. \quad (\text{S1})$$

Note the negative sign before the two-electron terms, i.e. the effective electron-electron interaction is attractive. Using Wick's theorem, the two-electron part of the Hamiltonian is approximated in the BCS treatment by a mean-field,

$$-V_{\mathbf{k}\mathbf{k}'} a_{\mathbf{k}\alpha}^\dagger a_{-\mathbf{k}\beta}^\dagger a_{-\mathbf{k}'\beta} a_{\mathbf{k}'\alpha} \approx -V_{\mathbf{k}\mathbf{k}'} \left(\langle a_{-\mathbf{k}\beta}^\dagger a_{-\mathbf{k}'\beta} \rangle a_{\mathbf{k}\alpha}^\dagger a_{\mathbf{k}'\alpha} - \langle a_{\mathbf{k}\alpha}^\dagger a_{-\mathbf{k}'\beta} \rangle a_{-\mathbf{k}\beta}^\dagger a_{\mathbf{k}'\alpha} + a_{\mathbf{k}\alpha}^\dagger a_{-\mathbf{k}\beta}^\dagger \langle a_{-\mathbf{k}'\beta} a_{\mathbf{k}'\alpha} \rangle \right), \quad (\text{S2})$$

where the first two terms are the normal Coulomb (J) and exchange (K) potentials, while the last term is the pairing potential. Writing the superconducting pair potential as

$$\Delta_{\mathbf{k}} = \sum_{\mathbf{k}'} -V_{\mathbf{k}\mathbf{k}'} \langle a_{-\mathbf{k}'\beta} a_{\mathbf{k}'\alpha} \rangle. \quad (\text{S3})$$

and absorbing the J and K terms, we obtain the mean-field BCS Hamiltonian for superconductivity,

$$\hat{H}^{\text{BCS}} = \sum_{\mathbf{k}} \left[\sum_{\sigma} (\varepsilon_{\mathbf{k}} - \mu) a_{\mathbf{k}\sigma}^\dagger a_{\mathbf{k}\sigma} + \left(\Delta_{\mathbf{k}} a_{\mathbf{k}\alpha}^\dagger a_{-\mathbf{k}\beta}^\dagger + \text{H.c.} \right) \right] + \text{const.} \quad (\text{S4})$$

To obtain the ground-state, we diagonalize this quadratic Hamiltonian using a Bogoliubov transformation [51, 52],

$$\begin{bmatrix} a_{\mathbf{k}\alpha} \\ a_{-\mathbf{k}\beta}^\dagger \end{bmatrix} = \begin{bmatrix} u_{\mathbf{k}} & v_{\mathbf{k}} \\ -v_{\mathbf{k}} & u_{\mathbf{k}} \end{bmatrix} \begin{bmatrix} p_{\mathbf{k}} \\ q_{\mathbf{k}}^\dagger \end{bmatrix}. \quad (\text{S5})$$

The new quasiparticles (p and q) mix particles and holes, and u and v are coefficients determined by the diagonalization and normalization conditions. In the new quasiparticle basis, the Hamiltonian becomes,

$$\hat{H}^{\text{BCS}} = \sum_{\mathbf{k}} E_{\mathbf{k}} (p_{\mathbf{k}}^\dagger p_{\mathbf{k}} + q_{\mathbf{k}}^\dagger q_{\mathbf{k}}) + \sum_{\mathbf{k}} (\varepsilon_{\mathbf{k}} - \mu - E_{\mathbf{k}}) + \text{const.}, \quad (\text{S6})$$

where

$$E_{\mathbf{k}} = \sqrt{(\varepsilon_{\mathbf{k}} - \mu)^2 + \Delta_{\mathbf{k}}^2}. \quad (\text{S7})$$

The order parameter $\Delta_{\mathbf{k}}$ is the also the gap function of the elementary excitations since $E_{\mathbf{k}} = |\Delta_{\mathbf{k}}|$ at the Fermi level ($\varepsilon = \mu$). The non-zero pairing also lowers the ground-state energy relative to the original fermion sea for any non-zero pairing. Thus an arbitrarily small attraction leads to the BCS ground-state.

In the current work, the BCS formalism enters the DMET calculation in an auxiliary way. In the DMET procedure, we self-consistently solve an interacting quantum impurity problem (with an interacting Hamiltonian \hat{H}^{emb} , and an

auxiliary mean-field problem, with Hamiltonian \hat{H}^{latt} . $\hat{H}^{\text{latt}} = \hat{\epsilon} + \hat{J} + \hat{K} + \hat{\Delta}$ can be viewed as a type of BCS Hamiltonian where the one-body operator $\hat{\epsilon}$, \hat{J} and \hat{K} come from a first principles calculation (with many bands) and $\hat{\Delta}$ is determined not by Wick's theorem, but by the DMET self-consistency with the interacting quantum impurity problem. In other words, finding the ground-state of H^{latt} corresponds to finding a BCS ground-state in a many-band picture, using a pair-potential supplied by the DMET self-consistency. (Note, however, that observables in DMET are computed using the ground-state of H^{emb} , not H^{latt}).

As mentioned in the main text, breaking particle number symmetry is inconvenient in quantum chemistry formulations. A formally equivalent alternative to working with the BCS ground-state and Hamiltonian is to redefine the vacuum so that the particle-number breaking terms become normal ones. We write

$$\begin{aligned}\hat{H}^{\text{BCS}} &= \sum_{\mathbf{k}} \begin{bmatrix} a_{\mathbf{k}\alpha}^\dagger & a_{-\mathbf{k}\beta} \end{bmatrix} \begin{bmatrix} \varepsilon_{\mathbf{k}} - \mu & \Delta_{\mathbf{k}} \\ \Delta_{\mathbf{k}}^\dagger & -\varepsilon_{\mathbf{k}} + \mu \end{bmatrix} \begin{bmatrix} a_{\mathbf{k}\alpha} \\ a_{-\mathbf{k}\beta}^\dagger \end{bmatrix} \\ &= \sum_{\mathbf{k}} \begin{bmatrix} c_{\mathbf{k}\alpha}^\dagger & c_{\mathbf{k}\beta}^\dagger \end{bmatrix} \begin{bmatrix} \varepsilon_{\mathbf{k}} - \mu & \Delta_{\mathbf{k}} \\ \Delta_{\mathbf{k}}^\dagger & -\varepsilon_{\mathbf{k}} + \mu \end{bmatrix} \begin{bmatrix} c_{\mathbf{k}\alpha} \\ c_{\mathbf{k}\beta} \end{bmatrix}.\end{aligned}\quad (\text{S8})$$

The second line is called the *Nambu representation*[30, 53], which effectively defines the following partial particle-hole (p-h) transformation,

$$\begin{aligned}c_{\mathbf{k}\alpha}^\dagger &= a_{\mathbf{k}\alpha}^\dagger \\ c_{\mathbf{k}\beta} &= a_{-\mathbf{k}\beta}^\dagger,\end{aligned}\quad (\text{S9})$$

The new vacuum of β particles is a ferromagnetic state where all the \mathbf{k} states are occupied by spin-down electrons, such that any further creation of β electrons will destroy the state. In the Nambu representation, the particle-number symmetry ($c^\dagger c$) becomes conserved at the expense of spin symmetry S_z breaking. Diagonalizing the quadratic Hamiltonian gives exactly the Bogoliubov coefficients in Eq. (S5). In quantum chemistry language, in the Nambu representation the Hamiltonian has a spin-coupling block Δ which mixes the two flavors of spin, similar to a spin-orbit coupling term. Therefore, we call this formulation a *generalized spin orbital* (GSO) formalism, which connects the superconducting problem to the treatment of spin-orbit coupling in quantum chemistry. We use the Nambu representation when formulating the *ab initio* quantum embedding procedure using GSOs in the next section.

We note that in the pair potential in Eq. (S3) we have assumed *singlet pairing* (strictly $S_z = 0$ pairing), i.e. the electron pair is composed of different spins with order parameter $\langle a_\alpha a_\beta \rangle$. It is also possible to have triplet pairing, where $\langle a_\alpha a_\alpha \rangle$ is non-zero. In that case, the Nambu representation can still be used, but the resulting Hamiltonian does not have the simple interpretation of generalized spin mixing (e.g., see [54, 55]). We will only consider singlet pairing in this work.

We next discuss pairing symmetry. We can view the order parameter Δ as the amplitude of a two-electron wavefunction. In the absence of spin-orbit coupling, a two-electron wavefunction can be decomposed into spatial and spin components,

$$\Psi(\mathbf{r}_1, \sigma_1, \mathbf{r}_2, \sigma_2) = \Delta(\mathbf{R}, \mathbf{r}) \chi(\sigma_1, \sigma_2), \quad (\text{S10})$$

where $\mathbf{R} = \mathbf{r}_1 + \mathbf{r}_2$ is the center of mass and $\mathbf{r} = \mathbf{r}_1 - \mathbf{r}_2$ is the relative coordinate. Assuming singlet pairing ($\langle \hat{S}^2 \rangle = 0$), the spin component $\chi(\sigma_1, \sigma_2) = -\chi(\sigma_2, \sigma_1)$ is anti-symmetric, and since the overall wavefunction is anti-symmetric, the spatial part Δ must be symmetric. Assuming the Hamiltonian is spatially rotationally invariant, we can classify Δ by the angular momentum quantum number l . The symmetric Δ then has even integer l , i.e. s ($l = 0$), d ($l = 2$), etc. The corresponding superconductor order parameters are called *s-wave*, *d-wave*, etc. respectively. In real materials, there is no continuous rotational invariance due to the lattice. One can, however, still classify the pairing symmetry using l by considering how the irreps reduce from the continuous rotational group to the point group associated with the cell. We note that in our calculations, the simultaneous presence of AFM order and SC order means that the order parameter breaks \hat{S}^2 symmetry, and this allows *p-wave* components to appear. We discuss the precise definition of the order parameters further in Sec. 1.5.

1.1.2 Ab initio superconducting Hamiltonians

In this section, we present useful formulae to build the Hamiltonians and matrix elements used in the DMET calculations, accounting for the additional steps of the Nambu transformation and subsequent normal ordering. As discussed in detail in Ref. [50], formally, we start with a second-quantized Hamiltonian in a crystal atomic orbital basis in the bulk lattice; the crystal atomic orbital basis gives rise to a set of one- and two-electron integrals labelled by the basis indices e.g. p, q, r, s , and \mathbf{k} -point indices $\mathbf{k}_p, \mathbf{k}_q, \dots$. We will use H_1 and V_2 to generically denote one-electron and two-electron integral tensors (for any Hamiltonian). DMET works with an embedding Hamiltonian \hat{H}^{emb} and a mean-field bulk Hamiltonian \hat{H}^{latt} and the matrix elements of these Hamiltonians are derived from the bulk H_1 and V_2 integrals through integral transformations and contractions with density matrices [50]. In the current work, in addition we need to perform the partial p-h transformation of the Nambu formalism,

$$\begin{aligned} c_{i\alpha}^{\dagger} &= a_{i\alpha}^{\dagger} \\ c_{j\beta} &= a_{j\beta}^{\dagger}. \end{aligned} \quad (\text{S11})$$

followed by normal ordering to obtain integrals in the quasiparticle representation, where we use calligraphic letters ($\mathcal{H}_1, \mathcal{V}_2$, etc) to denote the transformed quantities. After the Nambu transformation, all Hamiltonian components are particle-number conserving as used in generalized spin orbital quantum chemistry treatments.

- Overlap matrix and orbital coefficients

The partial p-h transform of the basis overlap matrix S (which may be different from the identity in the crystal atomic orbital basis) or orbital coefficients C reads,

$$S^{\mathbf{k}} \rightarrow \mathcal{S}^{\mathbf{k}} \equiv \begin{bmatrix} S^{\mathbf{k}} & 0 \\ 0 & S^{\mathbf{k}} \end{bmatrix}, \quad (\text{S12})$$

$$C^{\mathbf{k}} = \begin{bmatrix} C^{\alpha\mathbf{k}}, C^{\beta\mathbf{k}} \end{bmatrix} \rightarrow \mathcal{C}^{\mathbf{k}} \equiv \begin{bmatrix} C^{\alpha\mathbf{k}} & 0 \\ 0 & C^{\beta\mathbf{k}} \end{bmatrix}. \quad (\text{S13})$$

- One-body Hamiltonian

The partial p-h transform of a one-body Hamiltonian, $H_1^{\mathbf{k}}$, is

$$H_1^{\mathbf{k}} = \begin{bmatrix} h^{\alpha\mathbf{k}}, h^{\beta\mathbf{k}}, \Delta^{\alpha\beta\mathbf{k}} \end{bmatrix} \rightarrow \mathcal{H}_1^{\mathbf{k}} \equiv \begin{bmatrix} h^{\alpha\mathbf{k}} & \Delta^{\alpha\beta\mathbf{k}} \\ \Delta^{\alpha\beta\mathbf{k}\dagger} & -h^{\beta\mathbf{k}} \end{bmatrix} + \mathcal{H}_0, \quad (\text{S14})$$

where the energy constant $\mathcal{H}_0 = \sum_{\mathbf{k}} \text{Tr}(h^{\beta\mathbf{k}} S^{\mathbf{k}, -1})$ comes from the normal ordering (change of vacuum).

- One-body density matrix

The partial p-h transformation of a one-body reduced density matrix $\gamma_1^{\mathbf{k}}$ reads,

$$\gamma_1^{\mathbf{k}} = \begin{bmatrix} \gamma^{\alpha\mathbf{k}}, \gamma^{\beta\mathbf{k}}, \kappa^{\alpha\beta\mathbf{k}} \end{bmatrix} \rightarrow \mathcal{D}^{\mathbf{k}} \equiv \begin{bmatrix} \gamma^{\alpha\mathbf{k}} & \kappa^{\alpha\beta\mathbf{k}} \\ \kappa^{\alpha\beta\mathbf{k}\dagger} & S^{\mathbf{k}, -1} - \gamma^{\beta\mathbf{k}} \end{bmatrix}. \quad (\text{S15})$$

\mathcal{D} will serve as the *generalized density matrix* for constructing the embedding orbitals \mathcal{C} of DMET. The physical number of electrons (not the number of quasiparticles) can be computed as,

$$\begin{aligned} N^{\text{elec}} &= \frac{1}{N_{\mathbf{k}}} \sum_{\mathbf{k}} \text{Tr}\{\gamma^{\alpha\mathbf{k}} S^{\mathbf{k}}\} + \text{Tr}\{\gamma^{\beta\mathbf{k}} S^{\mathbf{k}}\} \\ &= \frac{1}{N_{\mathbf{k}}} \sum_{\mathbf{k}} \text{Tr}(\mathcal{D}^{\mathbf{k}} S^{\mathbf{k}})^{\alpha\alpha} + \text{Tr}(I - \mathcal{D}^{\mathbf{k}} S^{\mathbf{k}})^{\beta\beta} \end{aligned} \quad (\text{S16})$$

- Two-body Hamiltonian

The partial p-h transform of an electron repulsion integral (ERI), V_2 , is

$$V_2 \rightarrow \mathcal{V}_2 \equiv \begin{bmatrix} V & -V \\ -V^\dagger & V \end{bmatrix} + \mathcal{V}_1 + \mathcal{V}_0, \quad (\text{S17})$$

where

$$\mathcal{V}_1 = \begin{bmatrix} v^J & 0 \\ 0 & v^K - v^J \end{bmatrix} \quad (\text{S18})$$

with

$$\begin{aligned} v_{rs}^J &= \sum_{pq} S_{qp}^{-1} V_{pqrs}, \\ v_{ps}^K &= \sum_{qr} S_{qr}^{-1} V_{pqrs}, \end{aligned} \quad (\text{S19})$$

and

$$\mathcal{V}_0 = \frac{1}{2} \text{Tr}[(v_J - v_K) S^{-1}]. \quad (\text{S20})$$

- Two-body Hamiltonian from density fitting integrals

In realistic materials calculations, it is usually infeasible to store the entire two-electron integral tensor V_2 for the whole lattice. Instead, as discussed in Ref. [50], we use density fitting to obtain a low-rank decomposed V_2 expressed in terms of 3-center (crystal) atomic orbital (AO) integrals $W_{Lpq}^{\mathbf{k}_p \mathbf{k}_q}$, where L is an index in auxiliary density-fitting basis, and $p(q)$ are indices in the crystal AO computational basis (see Sec. 2.3 for details), and reconstruct the relevant V_2 integrals when needed. When constructing the V_2 or Fock matrix of the embedded problem, we never explicitly build the lattice V_2 (we only need to build \mathcal{V}_1 and \mathcal{V}_0). The relevant formulae are summarized in the following.

To construct \mathcal{V}_1 using density fitting, we use

$$\mathcal{V}_1^{\mathbf{k}} = \begin{bmatrix} v^{J\mathbf{k}} & 0 \\ 0 & v^{K\mathbf{k}} - v^{J\mathbf{k}} \end{bmatrix}, \quad (\text{S21})$$

where \mathbf{k} denotes the \mathbf{k} -point of interest, and $v^{J\mathbf{k}}$ is computed as

$$\rho_L = \frac{1}{N_{\mathbf{k}}} \sum_{\mathbf{k}pq} S_{qp}^{\mathbf{k},-1} W_{Lpq}^{\mathbf{k}\mathbf{k}}, \quad (\text{S22})$$

$$v_{rs}^{J\mathbf{k}} = \sum_L \rho_L W_{Lrs}^{\mathbf{k}\mathbf{k}}. \quad (\text{S23})$$

Similarly, $v^{K\mathbf{k}}$ is evaluated through

$$X_{Lqs}^{\mathbf{k}_q \mathbf{k}_p} = \sum_r S_{qr}^{\mathbf{k}_q, -1} W_{Lrs}^{\mathbf{k}_q \mathbf{k}_p}, \quad (\text{S24})$$

$$v_{ps}^{K\mathbf{k}_p} = \frac{1}{N_{\mathbf{k}}} \sum_{\mathbf{k}_q Lq} W_{Lqp}^{\mathbf{k}_q \mathbf{k}_p *} X_{Lqs}^{\mathbf{k}_q \mathbf{k}_p}. \quad (\text{S25})$$

The constant term is,

$$\mathcal{V}_0 = \frac{1}{2N_{\mathbf{k}}} \sum_{\mathbf{k}} \text{Tr}[(v^{J\mathbf{k}} - v^{K\mathbf{k}}) S^{\mathbf{k}, -1}]. \quad (\text{S26})$$

- Embedding Hamiltonian

The embedding orbitals (impurity \mathcal{I} + bath \mathcal{B}) are constructed via the SVD of the off-diagonal block of the generalized density matrix $\mathcal{D}^{\mathbf{R} \neq \mathbf{0}}$ [50],

$$\mathcal{D}^{\mathbf{R} \neq \mathbf{0}} = \mathcal{B}^{\mathbf{R} \neq \mathbf{0}} \Lambda V^\dagger, \quad (\text{S27})$$

where we have taken the first cell ($\mathbf{R} = \mathbf{0}$) as impurity. The embedding space (impurity + bath) are then spanned by the union of \mathcal{I} and \mathcal{B} ,

$$\mathcal{C}^{\mathbf{k}} = \sum_{\mathbf{R}} e^{-i\mathbf{k} \cdot \mathbf{R}} \mathcal{C}^{\mathbf{R}} = \sum_{\mathbf{R}} e^{-i\mathbf{k} \cdot \mathbf{R}} \begin{bmatrix} \mathcal{I}^{\mathbf{R}=\mathbf{0}} & \mathbf{0} \\ \mathbf{0} & \mathcal{B}^{\mathbf{R} \neq \mathbf{0}} \end{bmatrix}. \quad (\text{S28})$$

The construction of the embedding one-body Hamiltonian reads as,

$$\mathcal{H}_{ij}^{\text{emb}} = \frac{1}{N_{\mathbf{k}}} \sum_{\mathbf{k}} \mathcal{C}_{ip}^{\dagger} \mathcal{F}_{pq}^{\mathbf{k}} \mathcal{C}_{qj}^{\mathbf{k}} - (\mathcal{J}_{ij}[\mathcal{D}^{\text{emb}}] - \mathcal{K}_{ij}[\mathcal{D}^{\text{emb}}]) \quad (\text{S29})$$

where the generalized Fock matrix \mathcal{F} is projected using the embedding basis \mathcal{C} and subtracted by the double-counting embedding Coulomb (\mathcal{J}) and exchange (\mathcal{K}) contributions. These would require both the embedding density matrix,

$$\mathcal{D}^{\text{emb}} = \frac{1}{N_{\mathbf{k}}} \sum_{\mathbf{k}} \mathcal{C}^{\dagger} \mathcal{S}^{\mathbf{k}} \mathcal{D}^{\mathbf{k}} \mathcal{S}^{\mathbf{k}} \mathcal{C}, \quad (\text{S30})$$

and the embedding ERI,

$$\begin{aligned} \mathcal{V}_{ijkl}^{\text{emb}} = \frac{1}{N_{\mathbf{k}}} \sum_{\mathbf{k}_L} & \left(W_{Lij}^{\alpha\alpha\mathbf{k}_L\mathbf{00}*} W_{Lkl}^{\alpha\alpha\mathbf{k}_L\mathbf{00}} + W_{Lij}^{\beta\beta\mathbf{k}_L\mathbf{00}*} W_{Lkl}^{\beta\beta\mathbf{k}_L\mathbf{00}} \right. \\ & \left. - W_{Lij}^{\alpha\alpha\mathbf{k}_L\mathbf{00}*} W_{Lkl}^{\beta\beta\mathbf{k}_L\mathbf{00}} - W_{Lij}^{\beta\beta\mathbf{k}_L\mathbf{00}*} W_{Lkl}^{\alpha\alpha\mathbf{k}_L\mathbf{00}} \right), \end{aligned} \quad (\text{S31})$$

where the reference cell 3-center embedding integral W is calculated as,

$$W_{Lij}^{\sigma\tau\mathbf{k}_L\mathbf{00}} = \frac{1}{N_{\mathbf{k}}} \sum'_{\mathbf{k}_p\mathbf{k}_q} \sum_{pq} \mathcal{C}_{ip}^{\sigma\mathbf{k}_p\dagger} W_{Lpq}^{\mathbf{k}_p\mathbf{k}_q} \mathcal{C}_{qj}^{\tau\mathbf{k}_q}, \quad (\text{S32})$$

where \mathcal{C}^σ is the coefficient matrix of embedding orbitals with spin $\sigma = \{\alpha, \beta\}$ and the ' limits the summation through momentum conservation $\mathbf{k}_L = \mathbf{k}_p - \mathbf{k}_q + n\mathbf{b}$.

- Coulomb and exchange potential

The Coulomb \mathcal{J} and exchange \mathcal{K} potential in the quasiparticle representation is defined via a contraction between \mathcal{V}_2 and \mathcal{D}_1 ,

$$\mathcal{J}_{rs} = \sum_{pq} \mathcal{D}_{qp} \mathcal{V}_{pqrs}, \quad (\text{S33})$$

$$\mathcal{K}_{ps} = \sum_{qr} \mathcal{D}_{qr} \mathcal{V}_{pqrs}. \quad (\text{S34})$$

Substituting Eq. (S15) and (S17), we have

$$\begin{aligned} \mathcal{J}_{rs}^\alpha &= \sum_{pq} \mathcal{D}_{qp}^\alpha \mathcal{V}_{pqrs}^{\alpha\alpha} + \mathcal{D}_{qp}^\beta \mathcal{V}_{pqrs}^{\beta\alpha} \\ &= \sum_{pq} \mathcal{D}_{qp}^\alpha V_{pqrs} - \mathcal{D}_{qp}^\beta V_{pqrs} \\ &= \sum_{pq} \gamma_{pq}^\alpha V_{pqrs} + \gamma_{pq}^\beta V_{pqrs} - S_{pq}^{-1} V_{pqrs} \\ &= (\mathcal{T}(J^\alpha))_{rs} - v_{rs}^J, \end{aligned} \quad (\text{S35})$$

$$\begin{aligned}
\mathcal{J}_{rs}^\beta &= \sum_{pq} \mathcal{D}_{qp}^\beta \mathcal{V}_{pqrs}^{\beta\beta} + \mathcal{D}_{qp}^\alpha \mathcal{V}_{pqrs}^{\alpha\beta} \\
&= \sum_{pq} \mathcal{D}_{qp}^\beta V_{pqrs} - \mathcal{D}_{qp}^\alpha V_{pqrs} \\
&= \sum_{pq} -(\gamma_{pq}^\beta V_{pqrs} + \gamma_{pq}^\alpha V_{pqrs}) + S_{pq}^{-1} V_{pqrs} \\
&= (\mathcal{T}(J^\beta))_{rs} + v_{rs}^J.
\end{aligned} \tag{S36}$$

where we have defined a mapping operator \mathcal{T} for a matrix A to the Nambu representation: $\mathcal{T}(A^\alpha) = A^\alpha$ and $\mathcal{T}(A^\beta) = -A^\beta$. Note that this result is different from that obtained by directly transforming J using \mathcal{T} , because of the additional terms ($\mp v_{rs}^J$). When constructing the generalized Fock matrix \mathcal{F} , these additional terms, however, will be canceled out by adding \mathcal{V}_1 .

$$\begin{aligned}
\mathcal{K}_{ps}^\alpha &= \sum_{qr} \mathcal{D}_{qr}^\alpha \mathcal{V}_{pqrs}^{\alpha\alpha} \\
&= \sum_{qr} \mathcal{D}_{qr}^\alpha V_{pqrs} \\
&= \sum_{qr} \gamma_{qr}^\alpha V_{pqrs} \\
&= (\mathcal{T}(K^\alpha))_{ps},
\end{aligned} \tag{S37}$$

$$\begin{aligned}
\mathcal{K}_{ps}^\beta &= \sum_{qr} \mathcal{D}_{qr}^\beta \mathcal{V}_{pqrs}^{\beta\beta} \\
&= \sum_{qr} \mathcal{D}_{qr}^\beta V_{pqrs} \\
&= \sum_{qr} -\gamma_{qr}^\beta V_{pqrs} + S_{qr}^{-1} V_{pqrs} \\
&= (\mathcal{T}(K^\beta))_{ps} + v_{ps}^K.
\end{aligned} \tag{S38}$$

Note that this result is different from that obtained by directly transforming K using \mathcal{T} , because of the additional term (v_{ps}^K). This additional term is canceled out when adding with \mathcal{V}_1 .

$$\begin{aligned}
\mathcal{K}_{ps}^{\alpha\beta} &= \sum_{qr} \mathcal{D}_{qr}^{\alpha\beta} \mathcal{V}_{pqrs}^{\alpha\beta} \\
&= \sum_{qr} -\mathcal{D}_{qr}^{\alpha\beta} V_{pqrs} \\
&= \sum_{qr} -\kappa_{qr}^{\alpha\beta} V_{pqrs}.
\end{aligned} \tag{S39}$$

Note this term does not appear in the normal-state unrestricted Hartree-Fock (UHF) potential.

- Frozen-core approximation and DFT as the low-level theory

The frozen-core potential ($\mathcal{J}^{\text{core}}$ and $\mathcal{K}^{\text{core}}$) and core energy ($\mathcal{E}^{\text{core}}$) can be calculated using Eq. (S33) and (S34) with $\mathcal{D}^{\text{core}}$. In a density functional theory (DFT) Kohn-Sham Hamiltonian, the \mathcal{K} and v^K matrices should be ignored for pure functionals, or be scaled with the hybrid parameter of hybrid functionals (e.g., $x^{\text{hyb}} = 1/4$ in the PBE0 functional).

1.1.3 DMET algorithms for superconducting states

In this section, we discuss how to perform a DMET calculation of a doped cuprate. The following algorithm is implemented in `LIBDMET` [50, 22].

1. Set up the cell and the lattice. The doping requires modifying the total number of electrons in the cell (within either the rigid-band or virtual crystal approximation).
2. Mean-field calculation of the doped system (e.g., using unrestricted orbitals and the PBE0 functional as in this work).
3. Local (core, valence, and virtual) orbitals are constructed, $C^{\text{AO,core}}$, $C^{\text{AO,non-core}}$ (see Sec. 1.2 for details).
4. Partial p-h transform: Construct $\mathcal{C}^{\text{AO,core}}$, $\mathcal{C}^{\text{AO,non-core}}$, \mathcal{S} , \mathcal{H}_1 , \mathcal{H}_0 , \mathcal{V}_1 , \mathcal{V}_0 , $\mathcal{D}^{\text{core}}$, $\mathcal{J}^{\text{core}}$, $\mathcal{K}^{\text{core}}$, $\mathcal{E}^{\text{core}}$.

The resulting lattice Hamiltonian (all in a local orthogonal AO basis [50] without core orbitals, \mathbf{k} -point labels are omitted for clarity) is

$$\mathcal{H} = \mathcal{H}_1 + \mathcal{V}_1 + \mathcal{J}^{\text{core}} - x^{\text{hyb}} \mathcal{K}^{\text{core}} + \mathcal{E}, \quad (\text{S40})$$

where the constant term $\mathcal{E} = E^{\text{nuc}} + \mathcal{E}^{\text{core}} + \mathcal{H}_0 + \mathcal{V}_0$ includes the nuclear-nuclear repulsion energy, frozen-core energy, as well as the vacuum terms from the p-h transformation. Note that here \mathcal{V}_1 and \mathcal{V}_0 will also include a factor x^{hyb} if DFT is used.

The generalized Fock matrix comes from a direct transformation of the mean-field unrestricted DFT Kohn-Sham Fock matrices,

$$\mathcal{F} = \begin{bmatrix} F^\alpha & 0 \\ 0 & -F^\beta \end{bmatrix}. \quad (\text{S41})$$

To constrain the expectation value of the physical particle number, an additional chemical potential is included in \mathcal{H} and \mathcal{F} ,

$$\mathcal{M} = \begin{bmatrix} -\mu S & 0 \\ 0 & \mu S \end{bmatrix}. \quad (\text{S42})$$

5. Set up the correlation potential.

$$u^{\text{corr}} = \begin{bmatrix} 0 & \Delta^{\alpha\beta} \\ \Delta^{\alpha\beta\dagger} & 0 \end{bmatrix}. \quad (\text{S43})$$

The particle-number non-conserving part is from the correlation potential and is determined self-consistently through DMET. We also constrain the form of Δ to be a subset of local orbitals (the 3-band orbitals) and the point group symmetry (C_{2h}) is applied. The initial guess corresponds to a small d -wave potential among the four Cu $3d_{x^2-y^2}$ orbitals. In principle, we could also include the diagonal part in u^{corr} to determine the magnetic order self-consistently, but to reduce the complexity of the problem, we do not consider this degree of freedom in this work.

6. DMET main loop.

- Diagonalize the generalized lattice Fock matrix $\mathcal{F} + \mathcal{M} + u^{\text{corr}}$ to obtain the generalized density matrix \mathcal{D} and determine the lattice chemical potential μ that ensures the correct electron number (Eq. (S16)). Note that a small-temperature smearing (e.g., $\beta = \frac{1}{k_{\text{B}}T} = 1000$) is used at finite doping because the lattice Fock matrix gap is can be either small or vanishing.
- Construct the embedding (impurity + bath) orbitals \mathcal{C} from \mathcal{D} using Eq. (S27) and Eq. (S28).
- Construct the embedding Hamiltonian from the embedding orbitals \mathcal{C} and p-h transformed integrals[Eq. (S29) and (S31)]. Note that the DFT v^{xc} does not enter into the embedding Hamiltonian, only the Hartree-Fock embedding-core interaction, so there is no double-counting in the many-body solution.

(d) Solve the embedding problem with generalized solvers (e.g., the coupled cluster method introduced in Sec. 1.3). We also need to determine the chemical potential of the embedding problem μ^{emb} such that the physical electron number (Eq. (S16)) is the same as that obtained from the doped lattice (omitting the electron count from the core orbitals),

$$N^{\text{elec,emb}} = N^{\text{elec,latt without core}} \quad (\text{S44})$$

Currently, μ^{emb} is determined at the Hartree-Fock level.

(e) Compute \mathcal{D}^{emb} , transform it back to the original electron representation, and analyze the magnetic and pairing orders.

(f) Fit u^{corr} in the lattice problem by diagonalizing $\mathcal{F} + \mathcal{M} + u^{\text{corr}}$ and using least-squares correlation potential fitting. We only fit the anomalous part of the density matrix subblocks (3-band orbital subblocks of $\mathcal{D}^{\alpha\beta}$).

(g) Extrapolate \mathcal{D} and go back to (a) until the change $\|\mathcal{D}_{i+1} - \mathcal{D}_i\|$ is sufficiently small.

1.2 Localized orbitals for metallic systems

The ab initio DMET calculation is formulated in a local atomic orbital basis [50] constructed using the intrinsic atomic orbital (IAO) formalism [56]. The IAO formalism is usually formulated at zero-temperature, however, as discussed above we use finite-temperature smearing in the lattice problem, thus we need to extend the intrinsic atomic orbital construction to this case. We also discuss how to define the core IAOs in the frozen-core calculations.

- \mathbf{k} -adapted IAO [50]

IAO can be viewed as a set of AO-character based projected Wannier functions. The key ingredients for IAO construction are the occupied MOs $\{|\psi_m\rangle\}$ and two sets of pre-defined localized bases, B_1 and B_2 . B_1 is the normal AO basis used in the mean-field calculation (labeled by μ, ν, \dots) and B_2 is the reference minimal basis set (labeled by ρ, σ, \dots). B_1 usually contains the space of B_2 and the extra part reflects the polarization. The goal of IAO construction is to obtain a set of AO-like orbitals that contain the occupied space but have the size of the small basis set B_2 . To achieve this, we first define the *depolarized* MOs $\{|\bar{\psi}_m\rangle\}$ by projecting the MOs to B_2 , then back to B_1 ,

$$|\bar{\psi}_m\rangle = \text{orth}\left(P^{B_1} P^{B_2} |\psi_m\rangle\right), \quad (\text{S45})$$

where P is the resolution of identity (or projector) of AOs,

$$P_{\mu\nu}^{B_1} = \sum_{\mu\nu} |\phi_\mu\rangle S_{\mu\nu}^{B_1} \langle\phi_\nu|. \quad (\text{S46})$$

Using the depolarized MO projector $\bar{O} \equiv \sum_m |\bar{\psi}_m\rangle\langle\bar{\psi}_m|$, we can split the B_2 set into occupied ($\bar{O} |\phi_\rho\rangle$) and virtual spaces $(1 - \bar{O}) |\phi_\rho\rangle$. The IAOs $\{|\psi_i\rangle\}$ are obtained by further projecting these two subspace bases onto their polarized counterparts ($O \equiv \sum_m |\psi_m\rangle\langle\psi_m|$ and $1 - O$) and applying Löwdin orthogonalization,

$$|\psi_i\rangle = \text{orth}\{[O\bar{O} + (1 - O)(1 - \bar{O})] |\phi_\rho\rangle\}. \quad (\text{S47})$$

In periodic systems, the quantities in the above equations should be understood to carry \mathbf{k} labels, e.g. $|\phi_\mu\rangle \rightarrow |\phi_\mu^\mathbf{k}\rangle$ is a crystal AO, and $S^{B_1} \rightarrow S^{\mathbf{k}, B_1}$ is the corresponding overlap matrix. These quantities are already evaluated in the mean-field calculations. The only thing we need additionally is the overlap matrix S_{12} between basis B_1 and B_2 , which can be evaluated directly,

$$S_{\mu\rho}^{\mathbf{k}, B_1, B_2} = \sum_{\mathbf{T}} \int d\mathbf{r} e^{i\mathbf{k}\cdot\mathbf{T}} \phi_\mu^*(\mathbf{r}) \phi_\rho(\mathbf{r} - \mathbf{T}), \quad (\text{S48})$$

where the summation is over the periodic images \mathbf{T} . After the IAOs are constructed, the \mathbf{k} -adapted PAOs are obtained by projecting out the IAO components from the AOs at each \mathbf{k} -point.

- IAO with frozen-core orbitals

When dealing with frozen-core calculations, the construction of IAOs needs to be adjusted. The key idea is that B_1 basis now becomes a subset of MOs (i.e., only treat the non-core part of MOs), C_{pP} (we use capital letters P, Q, \dots for non-core indices). So the new occupied coefficients in the non-core basis become

$$C_{pm}^{\text{occ}} \rightarrow C_{Pm}^{\text{occ}} = \sum_{pq} C_{Pq}^{\dagger} S_{qp} C_{pm}^{\text{occ}}. \quad (\text{S49})$$

The large basis overlap S_1 matrix changes as

$$S_{pq} \rightarrow S_{PQ} = \sum_{pq} C_{Pp}^{\dagger} S_{pq} C_{qQ}. \quad (\text{S50})$$

Similarly, the inter-molecular overlap S_{12} reads,

$$S_{p\mu} \rightarrow S_{P\mu} = \sum_p C_{Pp}^{\dagger} S_{p\mu}. \quad (\text{S51})$$

The core and non-core IAOs are then constructed separately.

- IAO with finite-temperature smearing

For the large basis O , we can replace the occupied projector by a finite-temperature projector

$$O = \sum_m^{\text{occ}} |\psi_m\rangle \langle \psi_m| \rightarrow \sum_m |\psi_m\rangle f_m \langle \psi_m|, \quad (\text{S52})$$

where $f_m = \frac{1}{e^{\beta(\varepsilon_m - \mu)} + 1}$. The depolarized MO projector \bar{O} becomes,

$$\bar{O} = \sum_m^{\text{occ}} |\bar{\psi}_m\rangle \langle \bar{\psi}_m| \rightarrow \sum_{\varepsilon_m < \mu} |\bar{\psi}_m\rangle \langle \bar{\psi}_m|. \quad (\text{S53})$$

We cannot use the same formula in Eq. (S52) since $\{\bar{\psi}\}$ is not an orthogonal orbital set. Instead, we use the depolarized MOs below the Fermi level μ . This definition makes the IAOs still approximately span the “occupied space” of the smeared wavefunction. The deviation of the electron number trace in this IAO space (reflecting the inexact span of the occupied orbitals) is of order $1/\beta$.

1.3 Ab initio many-body impurity solver

As discussed above and in the main text, within the Nambu formulation, the DMET quantum many-body problem corresponds to the quantum chemistry problem of determining the ground-state of a Hamiltonian in the generalized spin-orbital language. The corresponding quantum chemistry solvers are then called “generalized” solvers. Below we describe three solvers used in this work: generalized coupled cluster with singles and doubles; generalized tailored coupled cluster with singles and doubles, and generalized ab initio density matrix renormalization group. Results from the tailored CC and ab initio DMRG solvers can be found in Sec. 3.1.

- Generalized coupled cluster

The main solver we use is the generalized coupled cluster singles and doubles (GCCSD) solver [57], which can be readily applied to *ab initio* embedding Hamiltonians with hundreds of orbitals. It is based on a wavefunction ansatz of the form

$$|\Psi\rangle = e^{\hat{T}_1 + \hat{T}_2} |\Phi\rangle, \quad (\text{S54})$$

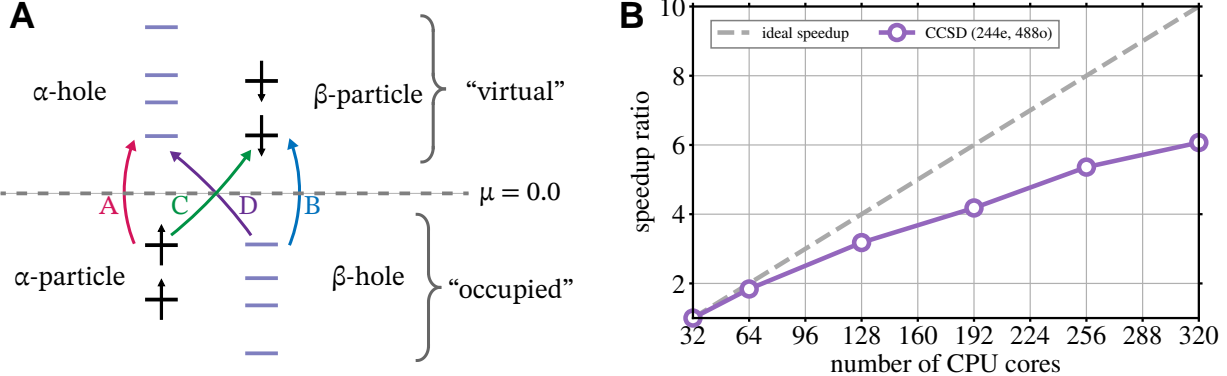


Figure S1: (A) Illustration of excitations in a superconducting state in the Nambu representation: The orbital space is split into occupied and virtual spaces. The ‘occupied’ orbitals arise from the mixing of α particles and β hole states; while the ‘virtual’ orbitals arise from the mixing of α holes and β particle states. The chemical potential $\mu = 0$. Different types of one-body excitations: A and B types of excitations are the normal-state particle-hole excitations, whereas C and D are superconducting types of excitation: C and D label the particle-particle and hole-hole channels respectively. (B) MPI parallel efficiency of generalized CCSD calculation in a half-filled cuprate impurity problem (488 spin orbitals).

where $|\Phi\rangle$ is a reference Slater determinant (a generalized HF determinant with a constrained average electron number) and the cluster excitation operators are defined as,

$$\begin{aligned}\hat{T}_1 &= \sum_{ia} t_i^a c_a^\dagger c_i, \\ \hat{T}_2 &= \frac{1}{4} \sum_{ijab} t_{ij}^{ab} c_a^\dagger c_b^\dagger c_j c_i.\end{aligned}\quad (\text{S55})$$

Since our orbitals are mixtures of particles and holes, the corresponding excitations contain both normal-state particle-hole type excitations, as well as superconducting type particle-particle (or hole-hole) excitations (as illustrated in Fig. S1A). The ‘occupied’ orbitals arise from the mixing of α particles and β hole states; while the ‘virtual’ orbitals arise from the mixing of α holes and β particle states. The whole spectrum is symmetric with respect to the chemical potential $\mu = 0$. In the limit of a non-superconducting state (pairing field $\Delta^{\alpha\beta} = 0$), the α -particle and β -holes are not mixed and the generalized Slater determinant calculation can be mapped onto an unrestricted Slater determinant.

In gapless or small gap problems, there can be difficulties converging the CCSD equations. The CCSD amplitudes are determined from the residual equations [26],

$$\begin{aligned}r_i^a &= \langle \Phi_i^a | e^{-\hat{T}_1 - \hat{T}_2} H e^{\hat{T}_1 + \hat{T}_2} | \Phi \rangle = 0, \\ r_{ij}^{ab} &= \langle \Phi_{ij}^{ab} | e^{-\hat{T}_1 - \hat{T}_2} H e^{\hat{T}_1 + \hat{T}_2} | \Phi \rangle = 0.\end{aligned}\quad (\text{S56})$$

Solving these equations is a non-linear root-finding problem and the standard method is to use Jacobian iteration with direct inversion of the iterative space (DIIS) [58]. This uses a preconditioner of the form

$$\mathcal{P} = \frac{1}{\varepsilon_i - \varepsilon_a} \propto \frac{1}{\text{gap}} \quad (\text{S57})$$

which does not work for small gap problems.

Various strategies can be employed to improve convergence, such as a regularized preconditioner,

$$\mathcal{P} = \frac{1}{\varepsilon_i - \varepsilon_a + \delta} \quad \text{or} \quad \frac{1}{\varepsilon_i - \varepsilon_a} (1 - e^{-\kappa(\varepsilon_i - \varepsilon_a)}). \quad (\text{S58})$$

We instead use a Newton-Krylov method, which approximates the inverse of the Jacobian \mathbf{J}^{-1} in a Krylov subspace and solves for the root in an inexact Newton way (we use a level-shift form of the preconditioner here as in Eq. (S58) with $\delta = 0.01$ a.u.). For the k^{th} iteration, the CCSD amplitudes \mathbf{t}^k are updated as,

$$\mathbf{t}^{k+1} = \mathbf{t}^k - \mathbf{J}^{-1} \mathbf{r}[\mathbf{t}^k]. \quad (\text{S59})$$

We have found this scheme to be more reliable for systems with near-orbital degeneracy than the traditional DIIS method [59, 60]. We implemented the Newton-Krylov GCCSD in the MPI4PySCF package with efficient MPI parallelism [61], see Fig. S1B for a cuprate impurity problem (488o, 244e) scaled up to 320 CPU cores.

As the CCSD method is inherently approximate in nature, it is important to evaluate its accuracy. To accomplish this, we benchmark the CCSD against the tailored coupled cluster method and the *ab initio* DMRG approach.

- Tailored coupled cluster

Tailored coupled cluster theory (TCC) was introduced as a method to treat systems with stronger correlation than can usually be treated by standard coupled cluster methods [62]. The basic idea is to treat part of the correlation by an exact method (full configuration interaction/exact diagonalization) and to treat the remaining correlation by the coupled cluster ansatz. The TCC wavefunction separates the cluster operators by categorizing them as either acting on the active (T_{act}) or external (T_{ext}) space of orbitals,

$$|\Psi\rangle = e^{\hat{T}_{\text{act}} + \hat{T}_{\text{ext}}} |\Phi\rangle \quad (\text{S60})$$

where the active space orbitals are the most strongly correlated ones. Specifically, in TCCSD theory, both \hat{T}_{act} and \hat{T}_{ext} are limited to single and doubles excitations,

$$\hat{T}_{\text{act}} = \hat{T}_{\text{act},1} + \hat{T}_{\text{act},2} \quad \hat{T}_{\text{ext}} = \hat{T}_{\text{ext},1} + \hat{T}_{\text{ext},2} \quad (\text{S61})$$

The active space component of the amplitudes is calculated using the full configuration interaction coefficients within the active space, corresponding to single and double excitations, c_i^a, c_{ij}^{ab} . Notably, these amplitudes are fixed in the calculation.

$$(t_{\text{act}})_i^a = \frac{c_i^a}{c_0}, \quad (t_{\text{act}})_{ij}^{ab} = \frac{c_{ij}^{ab}}{c_0} - \frac{c_i^a c_j^b - c_i^b c_j^a}{c_0^2} \quad a, b, i, j \in \text{act} \quad (\text{S62})$$

Coefficients corresponding to higher excitations within the active space are disregarded. The external component of the amplitudes is then determined by solving the amplitude equations consistent with Eq. (S56). The density matrix for the TCCSD method is computed in this study using the Lagrangian approach.

- Density matrix renormalization group

The *ab initio* density matrix renormalization group (DMRG) [63, 64] is regarded as a nearly exact method for quantum chemistry problems with several tens of orbitals. In this work, we use it as a benchmark tool to obtain an accurate solution of the impurity problem within a reduced active space of orbitals determined by the CC natural orbitals (the eigenvectors of CC density matrix) [65, 66].

1.4 Correlation potential matching between lattice and embedded impurity

In the self-consistent DMET cycle, we carry out self-consistency with respect to the superconducting order. We restrict the self-consistency to the (three-band block of) the anomalous part of the density matrix $\mathcal{D}^{\alpha\beta}$ of the lattice and embedding problems (although the pairing is non-zero outside of this block). We match the lattice and impurity orders using a least-squares fitting procedure [67], with an additional chemical potential to exactly match the electron number. In other words, after the embedding density matrix \mathcal{D}^{emb} is computed, we perform the minimization

$$\min_{u^{\text{corr}}} \|\mathcal{D}_{ij}^{\alpha\beta, \mathbf{R}=\mathbf{0}}[u^{\text{corr}}] - \mathcal{D}_{ij}^{\alpha\beta, \text{emb}}\| \quad (\text{S63})$$

where ij are limited to the three-band orbitals indices, and u^{corr} is the correlation potential on the three-band orbitals that obey C_{2h} point-group symmetry. $\mathcal{D}^{\mathbf{R}=\mathbf{0}}$ is obtained from the lattice Fermi-Dirac function,

$$(\mathcal{F}^{\mathbf{k}} + \mathcal{M} + u^{\text{corr}})\mathcal{C}^{\mathbf{k}} = \mathcal{C}^{\mathbf{k}}\mathcal{E}^{\mathbf{k}} \quad (\text{S64})$$

$$\mathcal{D}^{\mathbf{k}} = \mathcal{C}^{\mathbf{k}} \frac{1}{\exp(\mathcal{E}^{\mathbf{k}}/k_B T) + 1} \mathcal{C}^{\mathbf{k}\dagger} \quad (\text{S65})$$

The chemical potential μ in \mathcal{M} is additionally fitted during the minimization procedure to ensure the lattice problem always has the correct expectation value of the electron number (Eq. (S16)). To ensure the stability of this procedure, a small smearing temperature T is applied in lattice problem. The default temperature we use in this work is $\beta = 1000$. Additional results with $\beta = 2000$ and 5000 are given in Sec. 3.3.

1.5 Analysis methods

- Order parameters

In our work on the parent state [22], we defined charge, magnetic, and bond orders. We collect the relevant formulae here. The charge of local orbital i is,

$$n_i = \gamma_{ii}^{\alpha} + \gamma_{ii}^{\beta}, \quad (\text{S66})$$

and the local magnetic moment of orbital i is,

$$m_i = \gamma_{ii}^{\alpha} - \gamma_{ii}^{\beta}. \quad (\text{S67})$$

The 2-center Mayer bond order [68] between atoms A and B (or two subsets of orbitals) is defined as,

$$b_{AB} = \sum_{\sigma} b_{AB}^{\sigma} = 2 \sum_{\sigma} \sum_{i \in A} \sum_{j \in B} (\gamma^{\sigma} S)_{ji} (\gamma^{\sigma} S)_{ij}, \quad (\text{S68})$$

where γ^{σ} is the one-particle density matrix with spin σ and S is the overlap matrix of the local basis.

To characterize the SC order, we define real-space and orbital-resolved SC order parameters.

In one-band models and three-band Hubbard models, the SC order parameter is typically evaluated as the average of the Cu-Cu pairing components,

$$\begin{aligned} m_{\text{SC}} &= \sum_{\langle ij \rangle} \frac{1}{\sqrt{2}} \eta_{ij}^{\text{SC}} (\langle d_{i\alpha} d_{j\beta} \rangle + \langle d_{j\alpha} d_{i\beta} \rangle) \\ &= \sum_{\langle ij \rangle} \frac{1}{\sqrt{2}} \eta_{ij}^{\text{SC}} (\kappa_{ij}^{\alpha\beta} + \kappa_{ij}^{\alpha\beta\dagger}), \end{aligned} \quad (\text{S69})$$

where d denotes fermion operators on the Cu sites, and $\langle \dots \rangle$ limits the summation such that only the pairing between nearest Cu sites is taken into account. The d -wave superconducting structure factor η^{SC} is defined as

$$\eta_{i'i'}^{\text{SC}} = \begin{cases} +1, & \text{if } \mathbf{R}_i - \mathbf{R}_{i'} = \pm \mathbf{e}_x, \\ -1, & \text{if } \mathbf{R}_i - \mathbf{R}_{i'} = \pm \mathbf{e}_y. \end{cases} \quad (\text{S70})$$

where $\mathbf{e}_x(y)$ is the unit-cell lattice vector in the $x(y)$ direction. For s -wave Cu pairing, we use $\eta = 1$ for all terms.

In an *ab initio* calculation, it is interesting to explore the multi-orbital nature of the pairing. The above analysis can be extended to individual orbital-orbital pairing components by a suitable modification of the definition of the lattice vectors. However, it is useful to define a summarized version of the total pairing. Note that there is

no unique way to define this (as there are multiple ways to reduce to a single scalar). In this work, we define the total atomic pairing order, given a set of $\{\phi\}$ attached to each atom, as

$$\begin{aligned} m_{\text{SC}} &= \sum_{ij} \left| \sum_{\langle IJ \rangle} \frac{1}{\sqrt{2}} \eta_{IJ}^{\text{SC}} \left(\langle \phi_{i\alpha}^I \phi_{j\beta}^J \rangle + \langle \phi_{j\alpha}^J \phi_{i\beta}^I \rangle \right) \right| \\ &= \sum_{ij} \left| \sum_{\langle IJ \rangle} \frac{1}{\sqrt{2}} \eta_{IJ}^{\text{SC}} \left(\kappa_{ij}^{\alpha\beta IJ} + \kappa_{ij}^{\beta\alpha IJ} \right) \right|, \quad [\text{used in the main text}] \end{aligned} \quad (\text{S71})$$

where i (j) loops all of the local orbitals of atom I (J) and the phase factors η are the same as before. (Note that the intracell order is not included in the summation).

Besides Eq. (S71) (the main form of SC order we used in this work), we examine two other definitions of pairing order. One is to resolve the total pairing coupling of a given symmetry between unit cells. For example, in the 2×2 impurity, we can compute the angular momentum resolved orders as,

$$\begin{aligned} m^{s,\text{intra}} &= \sum_{\mathbf{R}=\mathbf{0},\mathbf{1},\mathbf{2},\mathbf{3}} \sum_{ij} \left| \frac{1}{\sqrt{2}} \left(\kappa_{ij}^{\mathbf{RR}} + \text{H.c.} \right) \right| \\ m^s &= \sum_{ij} \left| \frac{1}{\sqrt{2}} \left[\frac{1}{2} \left(\kappa_{ij}^{\mathbf{01}} + \kappa_{ij}^{\mathbf{12}} + \kappa_{ij}^{\mathbf{23}} + \kappa_{ij}^{\mathbf{30}} \right) + \text{H.c.} \right] \right| \\ m^{p_x} &= \sum_{ij} \left| \frac{1}{\sqrt{2}} \left[\frac{1}{\sqrt{2}} \left(\kappa_{ij}^{\mathbf{03}} - \kappa_{ij}^{\mathbf{30}} \right) + \text{H.c.} \right] \right| \\ m^d &= \sum_{ij} \left| \frac{1}{\sqrt{2}} \left[\frac{1}{2} \left(\kappa_{ij}^{\mathbf{01}} - \kappa_{ij}^{\mathbf{12}} + \kappa_{ij}^{\mathbf{23}} - \kappa_{ij}^{\mathbf{30}} \right) + \text{H.c.} \right] \right|, \end{aligned} \quad (\text{S72})$$

where $\mathbf{0}, \mathbf{1}, \mathbf{2}, \mathbf{3}$ are labels of unit cells in a 2×2 impurity. We show the angular momentum resolved components of the total order in Fig. S4B (see als for the cell arrangement).

We also study the real-space amplitude of the anomalous density matrix on the lattice

$$\kappa^{\alpha\beta}(\mathbf{R}_0, \mathbf{r}) = \sum_{ij} \phi_i^\alpha(\mathbf{R}_0) \kappa_{ij}^{\alpha\beta} \phi_j^{\beta*}(\mathbf{r}). \quad (\text{S73})$$

where \mathbf{R}_0 is chosen as a reference point near a Cu atom. This is visualized in Fig. 2C of the main text.

- Coupled cluster amplitudes decomposition

To understand the fluctuations driving pairing, we perform various analyses of the CCSD amplitude tensors t_i^a and t_{ij}^{ab} , where ij (ab) are occupied (virtual) orbital labels.

The first analysis is to check the correlation between the SC order and different blocks of CCSD amplitudes. As we have shown in Fig. S1A, the MOs are mixture of holes and particles and there is an arbitrary unitary rotation among occupied (or virtual) space. In order to label each MO with its largest character, we need to localize the occupied and virtual orbitals separately. The localization then re-mixes the orbital characters and gives a maximal separation between the α and β “spin” blocks. After the localization (by selected columns of density matrix, SCDM [69]), we can then attach each MO with a spin label. This analysis is valid for states where the particle-number-breaking sector is not large and the particle/hole characters can be largely disentangled.

After the localization procedure, the CCSD amplitudes then have block-wise structure. For instance, the T_1 amplitudes can be split into four blocks, as shown in Table S1. The first two blocks conserve the particle number while the third and fourth blocks change the particle number by 2, reflecting the superconducting pairing type excitations. Similarly, T_2 can be classified as normal and superconducting amplitudes based on the change in

Table S1: Decomposition of CCSD amplitudes based on the orbital character. The Frobenius norm values are taken from the calculation of CCO at normal pressure.

Amplitudes	i	a	j	b	particle number	norm
t_{α}^{α}	α (p)	α (h)			N	0.495
t_{β}^{β}	β (h)	β (p)			N	0.495
t_{α}^{β}	α (p)	β (p)			$N - 2$	0.084
t_{β}^{α}	β (h)	α (h)			$N + 2$	0.079
$t_{\alpha\alpha}^{\alpha\alpha}$	α (p)	α (h)	α (p)	α (h)	N	0.539
$t_{\alpha\beta}^{\alpha\beta}$	α (p)	α (h)	β (h)	β (p)	N	0.663
$t_{\alpha\beta}^{\beta\beta}$	α (p)	β (p)	β (h)	β (p)	$N - 2$	0.065
$t_{\alpha\alpha}^{\beta\beta}$	α (p)	β (p)	α (p)	β (p)	$N - 4$	0.004
...

particle number. The maximal change is 4. One can see that the main excitation is the normal-state particle-hole excitations, in particular the amplitude $t_{\alpha\beta}^{\alpha\beta}$ which includes the AFM type spin interactions. The main contribution in the superconducting blocks are of $N \pm 2$ particle number sector and $N \pm 4$ type excitations can be ignored.

The second analysis is the SVD decomposition of T_2 amplitudes. To explain our procedure, it is useful to establish the correspondence between T_2 amplitudes in the Nambu representation and without the Nambu transformation, thus we first assume that there is no pairing field. Then the initial generalized Hartree-Fock ground-state in the Nambu representation is the same as an unrestricted Hartree-Fock ground-state of the original electrons. Using the Nambu creation and annihilation basis (c^{\dagger}, c) , the \hat{T}_2 operator is

$$\hat{T}_2 = \frac{1}{4} \sum_{ijab} t_{ij}^{ab} c_a^{\dagger} c_b^{\dagger} c_j c_i \quad (S74)$$

where i, j are the Nambu “occupied” indices, and a, b are the Nambu “virtual” indices (see Fig. S1A). Through the particle-hole transformation, we see that $c_i \in \{a_{I\alpha}, a_{A\beta}^{\dagger}\}$ and $c_a^{\dagger} \in \{a_{A\alpha}^{\dagger}, a_{J\beta}\}$, where I, J are the electron occupied orbital indices, and A, B are electron virtual indices. Then, for pairs of fermionic operators, we have relations like

$$\begin{aligned} c_i c_a^{\dagger} &\in \{a_{I\alpha} a_{A\alpha}^{\dagger}, a_{I\alpha} a_{J\beta}, a_{A\beta}^{\dagger} a_{A\alpha}^{\dagger}, a_{A\beta}^{\dagger} a_{J\beta}\} \\ c_i c_j &\in \{a_{I\alpha} a_{J\alpha}, a_{I\alpha} a_{A\beta}^{\dagger}, a_{A\beta}^{\dagger} a_{B\beta}^{\dagger}, a_{A\beta}^{\dagger} a_{I\alpha}\} \\ &\dots \end{aligned} \quad (S75)$$

where the first pair operator $c_i c_a^{\dagger}$ contains 4 types of single excitations (see also Fig. S1A and the t_1 amplitudes in Table S1), where all of them conserve spin ($\Delta S_z = 0$), whereas the second pair $c_i c_j$ changes spin ($\Delta S_z = -1$). If there is a pairing field (so that the generalized Hartree-Fock ground-state is no longer mappable onto an unrestricted Hartree-Fock ground-state) then c_i and c_a^{\dagger} become linear combinations of their electron particle and electron hole components, but this does not change the spin nature of the pair operators $c_i c_j, c_i c_a^{\dagger}$.

Thus, we can consider two different SVD decompositions of T_2 from grouping the indices in two ways:

$$\begin{aligned} t_{ia,jb} &= \sum_s U_{ia,s}^0 \Sigma_s^0 V_{s,jb}^{0\dagger} \text{ (spin conserving),} \\ t_{ij,ab} &= \sum_s U_{ij,s}^{\pm 1} \Sigma_s^{\pm 1} V_{s,ab}^{\pm 1\dagger} \text{ (spin fluctuating).} \end{aligned} \quad (S76)$$

Using these singular values, we rewrite \hat{T}_2 ,

$$\hat{T}_2 = \sum_s \Sigma_s^0 \hat{O}_s^0 \hat{O}_s^0 \text{ (spin conserving)}, \quad (\text{S77})$$

$$\hat{T}_2 = \sum_s \Sigma_s^{\pm 1} \hat{O}_s^{\pm 1} \hat{O}_s^{\pm 1} \text{ (spin fluctuating)}. \quad (\text{S78})$$

We can then check to see if the spectrum of singular values of Σ is dominated by a few modes in the spin-conserving or spin-fluctuating decomposition, and we can also analyze the dominant singular vectors to see their effects on the charge and magnetic density. This type of fluctuation analysis is analogous to that performed for two-particle Green's functions e.g. in [48]. Alternatively, some related intuition is provided by a ground-state random phase approximation (RPA) analysis. Regarding the \hat{O} above as (quasi)bosonic operators, we see that in the RPA, the \hat{T}_2 CC wavefunction can be written as

$$|\Psi\rangle = e^{\frac{1}{2} \sum_{\mu\nu} t_{\mu\nu} b_\mu^\dagger b_\nu^\dagger} |0_B\rangle \quad (\text{S79})$$

where b is a bosonic operator (defined on the boson vacuum $|0_B\rangle$). Then, the above effects a canonical transformation, where the rotated particles (from the T amplitude rotation) are

$$\tilde{b}_\mu = \sum_\nu \left([1 - t^2]_{\mu\nu}^{1/2} b_\nu + ([1 - t^2]^{1/2} t)_{\mu\nu} b_\nu^\dagger \right) \approx b_\mu + \sum_\nu t_{\mu\nu} b_\nu^\dagger \quad (\text{S80})$$

A dominant singular value in $t_{\mu\nu}$ thus defines a main bosonic degree of freedom that is “mixed in” to the original degrees of freedom.

2 Computational details

2.1 Atomic modelling of doping

The hole or electron doping of cuprates is usually generated by chemical doping, which involves substituting buffer layer ions or introducing additional ions. For example, La_2CuO_4 is typically doped by replacing some of the La (III) ions with Sr (II) ions; because the entire crystal remains neutral, this means that charge must be taken out of the cuprate plane, effectively doping the plane with holes. Another example particularly relevant to this work is the hole doping of Hg-based cuprates, where oxygen is introduced into the Hg buffer layer, whose charge must then be compensated by other ions, including from the CuO_2 plane. Note that the effective doping of the CuO_2 plane is not always simple to determine from the dopant atom concentration alone, as charge can be redistributed across many different atoms. Consequently, the best way to simulate chemical doping is to use explicit dopant atoms. Unfortunately, the corresponding supercells become large and thus difficult to treat.

A simple way to dope without using explicit dopants is provided by the *rigid band approximation* (RBA). In this case, one directly removes or adds charge to the system, and assumes that there is a neutralizing background charge. This is similar in spirit to doping in lattice models, which is performed simply by modifying the number of particles.

Another method is the *virtual crystal approximation* (VCA) [70, 29], where the nuclear potential is obtained by mixing different site compositions, e.g. if a lattice site has x probability being occupied by atom A, and $(1 - x)$ probability by atom B, the VCA nuclear potential is defined as,

$$\bar{H}_{\text{nuc}}^{\text{VCA}}(\mathbf{r}) = x V_{\text{nuc}}^{\text{A}}(\mathbf{r}) + (1 - x) V_{\text{nuc}}^{\text{B}}(\mathbf{r}). \quad (\text{S81})$$

This approximation is still very crude as one can imagine that the effect of a half-occupied oxygen ($Z = 8$) site is fundamentally different to the potential from a Be atom ($Z = 4$).

In the current work, we mainly use the RBA treatment of doping with VCA applied in a few cases as an additional benchmark. Results from the VCA treatment of CCO at different pressures are presented in Sec. 3.2.

We enforce a neutral total lattice and we consider crystals where the total number of electrons (summed over all sampled \mathbf{k} points) is an even integer (the number of electrons per cell can obviously be a fractional number). We use

a 2×2 supercell to allow superconducting orders. If we define the doping concentration as the number of additional charges per Cu, then this allows a minimal doping of $1/(4n_k)$, where 4 is the number of Cu per cell. For the VCA calculations on CCO, the VCA potential mixing was carried out at the Ca ion, whose nuclear charge was modified according to the doping.

2.2 Optimization of Gaussian basis sets

To enable compact and numerically well-conditioned calculations on the materials in this work, we optimized a new set of Gaussian bases. The structure of the Gaussian basis sets for Ca, Cu, Ba, La, and Hg used in this work is summarized in Table S2. These basis sets are of double-zeta quality and generated for the GTH pseudopotentials [71, 72] optimized for HF calculations [73] by following a protocol modified from Ref. [74], which is outlined below. The Gaussian basis sets for all other elements are taken from Ref. [74].

1. A series of uncontracted valence basis sets of different sizes is generated by minimizing the HF ground-state energy of a free atom. For Ca and Cu, where the $[4p]$ shell is unoccupied in the HF ground state, we use the ground-state CCSD correlation energy of a free atom. A similar treatment is applied for the $[6p]$ shell of Ba, La, and Hg.
2. For a given uncontracted valence basis, a series of polarization basis sets of different sizes is generated by minimizing the ground-state CCSD correlation energy of a free atom.
3. A series of full uncontracted basis sets (valence + polarization) is generated by combining the valence basis sets and the polarization basis sets obtained in the previous steps. The full uncontracted basis sets whose overlap matrix condition number evaluated for the reference solids listed in Table S3 is less than 10^{10} are kept.
4. For the full uncontracted basis sets surviving the previous step, the one that minimizes the average error of the atomization energy of the reference molecules listed in Table S3 is selected (the error is calculated against a large basis set discarded in the previous step.)
5. The selected full uncontracted basis set is contracted using the coefficients of the spherically averaged CCSD atomic natural orbitals [75]. Different contraction patterns have been tested, and the one that minimizes the average error of the molecular atomization energy is selected to make the final contracted basis set.

Table S2: Summary of the optimized Gaussian basis sets used in this work. Valence configuration refers to the electrons not frozen in the chosen GTH pseudopotentials. The structure of both the uncontracted (denoted by parenthesis) and contracted (denoted by bracket) basis sets are listed for both the valence basis and the polarization basis. The structure of the final contracted basis set is also included.

Element	Valence configuration	Valence basis	Polarization basis	Final contracted basis
Ca	$[3s^2 3p^6 4s^2]$	$(5s, 5p) \rightarrow [3s, 3p]$	$(5d) \rightarrow [2d]$	$[3s, 3p, 2d]$
Cu	$[3s^2 3p^6 3d^{10} 4s^1]$	$(5s, 6p, 4d) \rightarrow [3s, 3p, 2d]$	$(2f) \rightarrow [1f]$	$[3s, 3p, 2d, 1f]$
Ba	$[5s^2 5p^6 6s^2]$	$(5s, 6p) \rightarrow [3s, 3p]$	$(6d) \rightarrow [2d]$	$[3s, 3p, 2d]$
La	$[5s^2 5p^6 5d^1 6s^2]$	$(6s, 6p, 3d) \rightarrow [4s, 3p, 2d]$	$(4f) \rightarrow [1f]$	$[4s, 3p, 2d, 1f]$
Hg	$[5d^{10} 6s^2]$	$(4s, 4p, 5d) \rightarrow [3s, 3p, 3d]$	$(2f) \rightarrow [1f]$	$[3s, 3p, 3d, 1f]$

We tested different bases on CCO using unrestricted PBE0. From Fig. S2, it is clear that the all bases beyond the single- ζ level provide reasonable Birch-Murnaghan (B-M) equations of state (EOS) [76, 77]. The single- ζ basis (GTH-SZV), however, is too small to give the correct EOS.

In terms of the magnetic properties, the magnetic moment decreases when pressure increases (volume decreases) and the magnetic coupling J increases. In the single- ζ basis the first trend is reversed, although the J trend is qualitatively correct. The GTH-DZVP basis has a qualitatively correct trend but the absolute value of J (141 meV) is still far away from the plane-wave reference number (217 meV). The new optimized GTH-cc-pVDZ basis and

Table S3: Reference solids and molecules used for determining the size and contraction pattern of the basis sets developed in this work.

Element	Reference solids	Reference molecules
Ca	CaO, CaF ₂	CaH, CaH ₂ , CaF, CaF ₂ , CaO, CaS
Cu	Cu (fcc), CuF, CuO	CuH, CuH ₂ , CuH ₃ , CuF, CuF ₂ , CuO, CuOF, CuS
Ba	BaO, BaF ₂	BaH, BaH ₂ , BaF, BaF ₂ , BaO, BaS
La	LaN, La (fcc/hcp), La ₂ O ₃	LaH, LaH ₂ , LaH ₃ , LaF, LaF ₂ , LaF ₃ , LaO, LaN, LaS
Hg	HgO, Hg (fcc), HgS	HgH, HgH ₂ , HgF, HgF ₂ , HgO, HgS

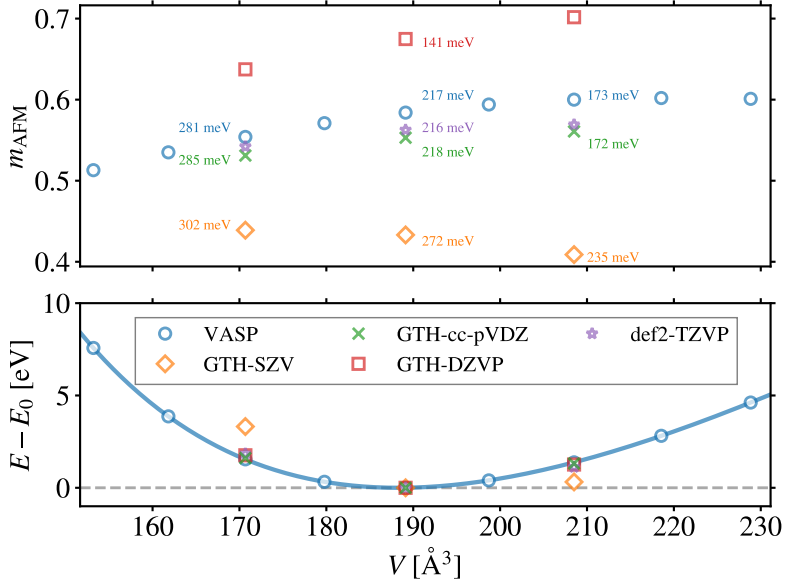


Figure S2: Mean-field basis check of the equation of state, magnetic moment m_{AFM} and magnetic exchange coupling J of CCO using unrestricted PBE0. Correspondings J 's are given by the labels.

the all-electron triple- ζ -level def2-TZVP basis are both in good agreement with the plane-wave reference (error in $\Delta J < 5$ meV). This confirms that the double- ζ level GTH-cc-pVDZ basis in this work provides a good balance between accuracy and efficiency.

2.3 Mean-field settings

The single particle mean-field (SCF) calculations (HF, DFT) were carried out using the crystalline Gaussian atomic orbital basis representation in the PySCF package [78, 79]. The results of these calculations were cross-checked against plane wave basis calculations using the VASP package [80, 81, 82, 83, 84].

For CCO and the Hg-based cuprates, we used the correlation consistent double- ζ basis GTH-cc-pVDZ defined above, using the GTH pseudopotential for the core electrons [71, 72]. Gaussian density fitting was used to compute the two-electron integrals. We used a specially-optimized Gaussian basis as the density fitting auxiliary basis for Cu, O and Ca; and used the def2-TZVP-RI basis for the auxiliary basis of Hg and Ba ($n_{\text{aux}} \sim 5n_{\text{AO}}$).

For the plane wave basis calculations, a projector-augmented wave (PAW) [85, 84] representation was used to treat the core electrons and we used a plane wave kinetic energy cutoff of 500 eV.

We sampled the Brillouin zone with a Γ -centered \mathbf{k} mesh: we used $4 \times 4 \times 2$ for the 2×2 supercell of the single layer compounds CCO and Hg-1201; $4 \times 4 \times 1$ for the 2×2 supercell of the double-layer compound Hg-1212.

All mean-field calculations used a Fermi-Dirac smearing of 0.2 eV. All mean-field calculations were converged to an accuracy of better than 10^{-8} a.u. per unit cell.

We used the PBE0 [86] hybrid functional for all doping RBA and VCA concentrations. All calculations were spin-unrestricted so that the AFM order could be stabilized at the DFT level. HF calculations were also performed, but we found that these gave very poor descriptions of the doped states.

In general, it is important to note that the basic features of the charge density are established by the choice of mean-field and the choice of doping representation rather than the DMET self-consistency, as the self-consistency is performed here on the anomalous part of the correlation potential.

2.4 DMET settings

All DMET routines, including the bath construction, integral transformation, solver interface, and correlation potential fitting, were implemented in the `LIBDMET` package [50, 87]. To remove core orbitals (which make the bath construction unstable and increases the computational cost) we froze the lowest mean-field bands ($3s3p$ bands for Cu and Ca, $2s$ bands for O, $5s$ bands for Ba); and we also froze the Cu $4f$ and O $3d$ virtuals to further reduce the cost.

We added the correlation potential u to the CuO_2 three-band orbitals and *only* fitted the three-band orbital anomalous blocks of the density matrices, i.e., $\langle a_{i\alpha} a_{j\beta} \rangle$ where $ij \in$ three-band orbitals (the self-consistency of the normal magnetic part is not considered in this work). We also enforced C_{2h} symmetry in u . The initial guess of u was chosen as a d -wave pattern on Cu $3d_{x^2-y^2}$ orbitals with a small amplitude 10^{-3} . The convergence criterion on the DMET self-consistency was chosen such that the maximal change of an element in u was less than 5×10^{-4} a.u..

In the DMET mean-field and correlation fitting, a small smearing of $\beta = 1/k_B T = 1000$ a.u. was added to the lattice.

We used the Newton-Krylov CCSD methods implemented in MPI4PYSCF [61] as solvers. The CCSD T and Λ equations were converged to a residual of less than 10^{-4} a.u. The largest embedding problem we treated using the CCSD solver was of size (376o, 188e), with multiple such size fragments solved simultaneously in the multi-fragment embedding formalism.

For TCCSD, we use an active space of 16 spin orbitals, defined from the CCSD natural orbitals. The active space was solved by the exact diagonalization.

Ab initio DMRG in the generalized spin orbital formalism was implemented in `BLOCK2` package [88]. A series of active spaces of 16, 32, 48, 64 orbitals (using CCSD natural orbitals in the last DMET iteration) were solved by DMRG with a maximal bond dimension $M = 3000$.

3 Additional data

3.1 Ab initio impurity solver benchmarks and order parameters

Fig. S3 shows AFM order and d -wave pairing order computed using a 2×2 plaquette impurity embedded in the 1-band 2D Hubbard model using an exact diagonalization (FCI) solver and the CCSD solver. (Note that this data is intended to test the quality of the CCSD solver, rather than report on the detailed physics of the 2D Hubbard model). As can be seen, the CCSD solver provides a quantitatively accurate impurity solver for the magnetic order at all dopings. The pairing order from the CCSD solver is slightly less accurate, but still shows quite good agreement with the exact diagonalization solver up to $U = 6$. The main discrepancy from ED at $U = 8$ is the width of the SC dome, which is narrower when using the CCSD solver.

In Fig. S4A we show the Cu d -wave order parameter as a function of doping for CCO at ambient pressure using several different solvers. The full orbital space for the CCO impurity consists of 376 orbitals. In the DMRG calculations, we solve the impurity problem from the last iteration of the DMET self-consistency (using the CCSD solver), but reduce the impurity problem orbital size (using coupled cluster natural orbitals) to active spaces of 16-64 orbitals. We see that the order parameter produced by DMRG is in good agreement with that obtained from CCSD. The TCCSD calculations used a 16 orbital active space to fix the active space amplitudes, but otherwise correlated all orbitals, and were performed with full DMET self-consistency. We see that these are also in good agreement with the results from the CCSD solver performed with DMET self-consistency. Taken together with the benchmark data generated on the Hubbard model on SC order with the CCSD solver, as well as multiple studies of the accuracy of the CCSD solver for magnetic order parameters in transition metal oxide materials [89, 22, 90, 50], we expect the trends in this work to be adequately reproduced using the CCSD solver.

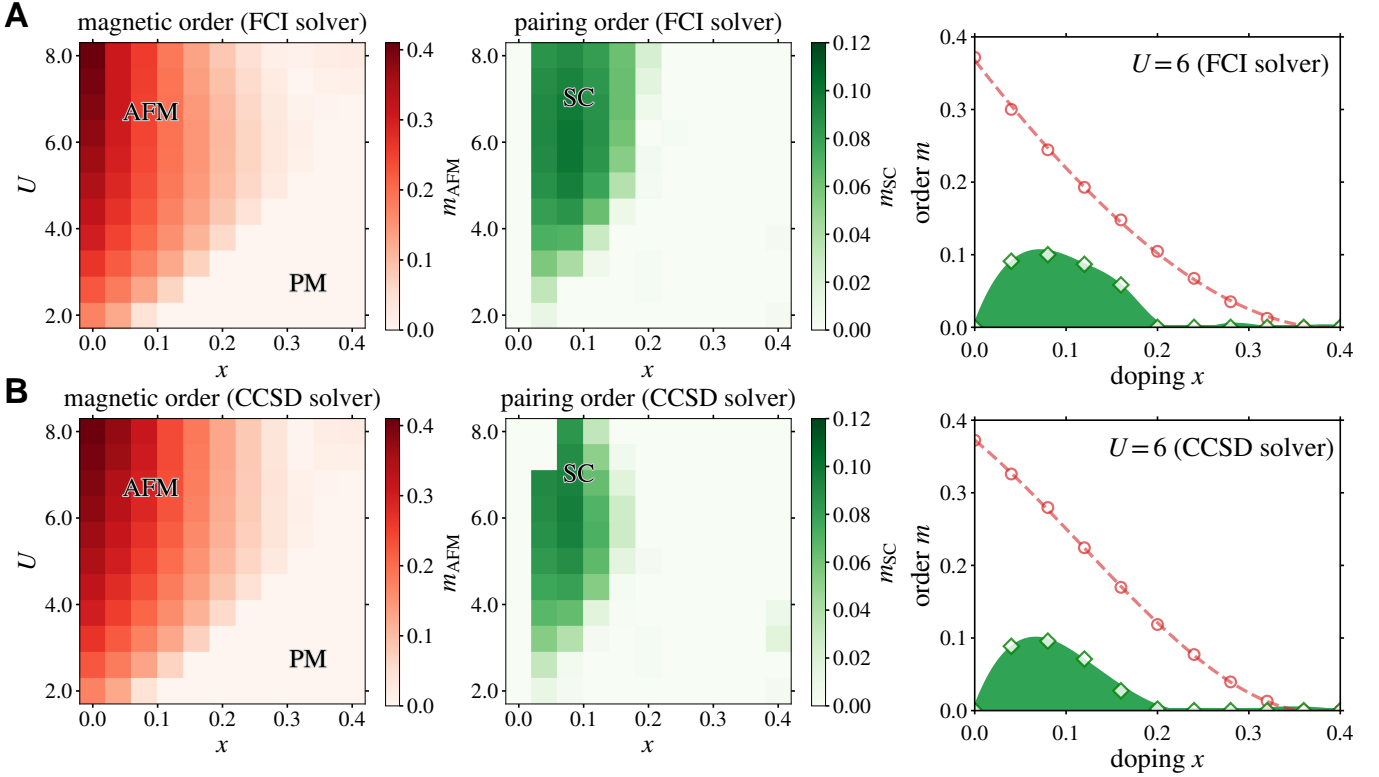


Figure S3: **Benchmark of impurity solver on the phase diagram of the one-band Hubbard model.** A 2×2 impurity is embedded in 40×40 square lattice. The figure plots the magnetic (AFM, paramagnetic (PM)) and pairing order (d -wave) for different U and doping x from (A) FCI (exact diagonalization) solver and (B) CCSD solver.

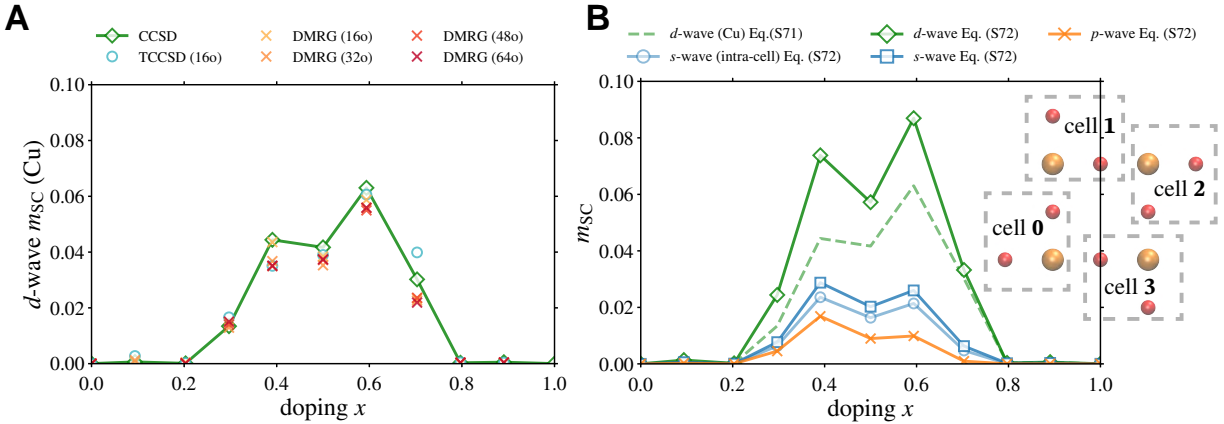


Figure S4: **Benchmark of impurity solver and definitions of order parameter.** (A) Comparison between different solvers (for CCO at normal pressure): CCSD, tailored CCSD with active space of 16 orbitals. DMRG active space calculations of 16 - 64 orbitals. The active spaces are spanned from the CCSD natural orbitals near the Fermi level. (B) Comparison between different definitions of pairing order parameter. Using Eq. (S72), we calculated s , p , d -wave component of order parameters among 4 unit cells in the 2×2 impurity. The d -wave pairing order between 4 Cu's (using Eq. (S71)) is shown by the dashed line.

In Fig. S4B we show additional data giving the decomposition of the total pairing order into intra-cell and inter-cell components in CCO at ambient pressure (using Eq. (S72)). In Fig. S5 and S6 we show the orbital-resolved d - and s -wave orders (using Eq. (S71)).

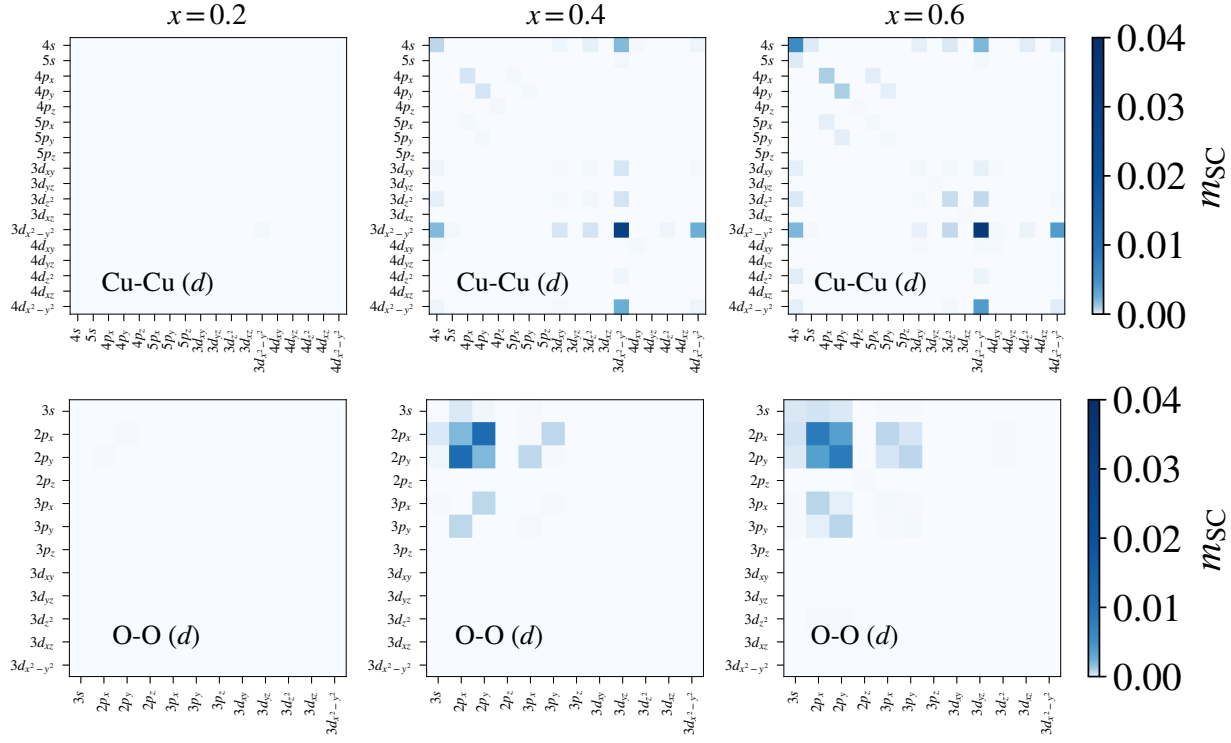


Figure S5: Orbital-resolved d -wave order parameter of CCO at ambient pressure for Cu-Cu and O-O orbital pairs ($4f$ orbitals are omitted for clarity).

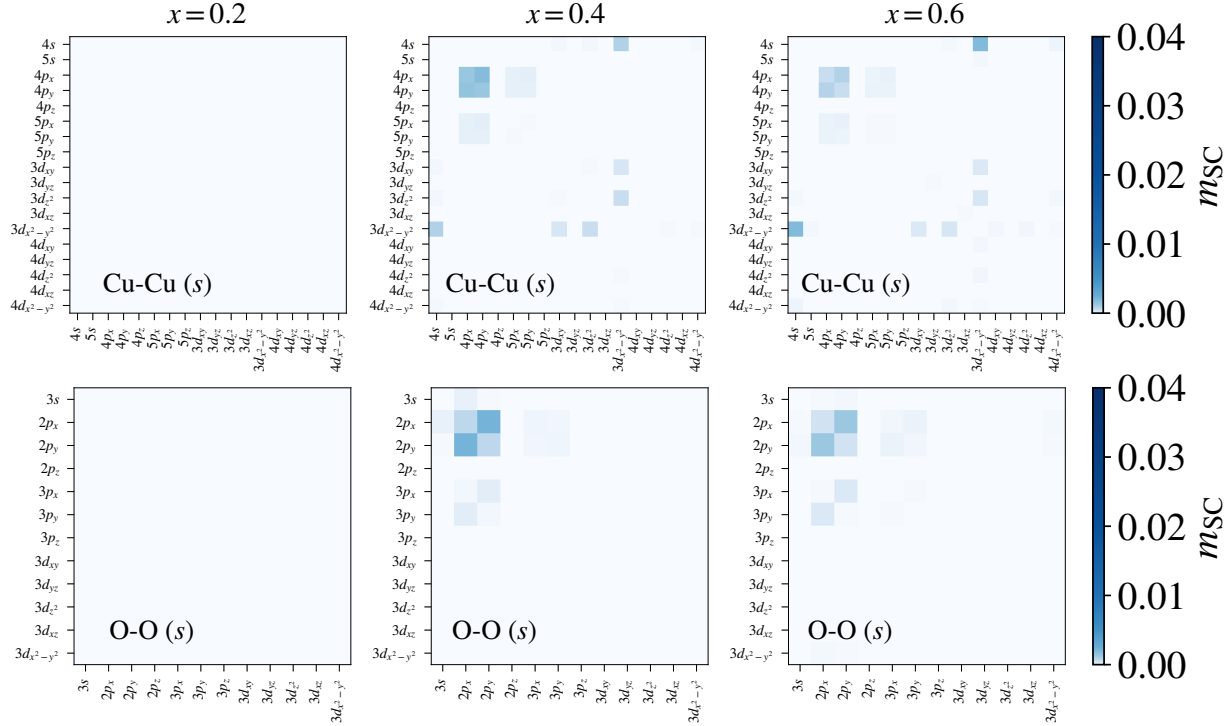


Figure S6: Orbital-resolved s -wave order parameter of CCO at ambient pressure for Cu-Cu and O-O orbital pairs ($4f$ orbitals are omitted for clarity).

3.2 Virtual crystal approximation data

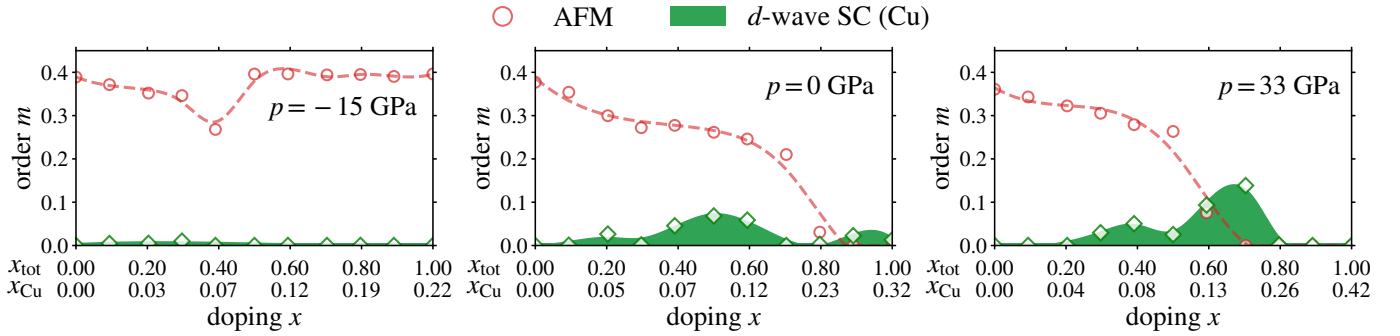


Figure S7: Pressure effect on hole-doped CCO using DMET @ VCA.

In Fig. S7 we show results from the VCA for CCO at different pressures. The general features, such as the decay of the AFM order, the emergence of the SC dome(s), the increase of the SC strength under pressure, are almost the same as with the RBA (Fig. 2 in the main text). This indicates the robustness of the pressure trend. One interesting feature is that in the VCA, the SC order is very weak in the negative pressure case, possibly owing to the fact that fewer holes go to the CuO_2 plane as compared to the RBA, leading to a lower effective Cu doping.

3.3 Influence of lattice smearing temperature

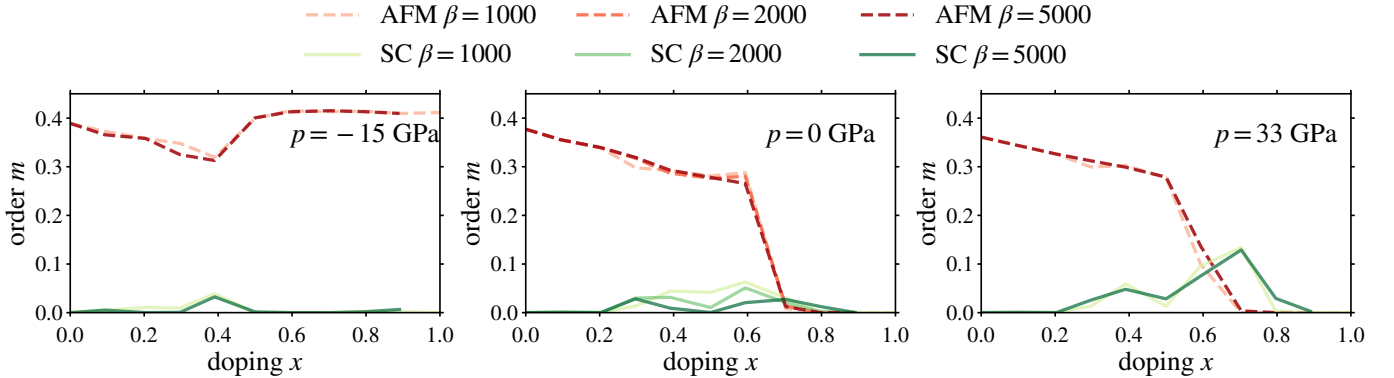


Figure S8: CCO with RBA using different lattice temperatures $\beta = \frac{1}{k_B T} = 1000, 2000, 5000$ a.u..

The finite temperature smearing is used to help the DMET fitting and self-consistency converge: in general, the fitting and convergence becomes harder at lower temperatures. We see that there are some quantitative differences at ambient pressure due to the finite temperature smearing, however, the basic trend in maximum pairing order is reasonably robust.

3.4 Comparison between reduced and oxidized structures of Hg-1212

Table S4: Properties of reduced (red) and oxidized (ox) structures of Hg-1212 using DFT (PBE0).

Structure doping	Hg-1212 (red)		Hg-1212 (ox)	
	$x = 0.0$	$x = 0.5$	$x = 0.0$	$x = 0.5$
V [Å ³]	757.9		752.9	
d Cu-O in-plane [Å]	1.932		1.928	
d Cu-O apical [Å]	2.824		2.775	
m_{AFM} (\mathbf{k} - $4 \times 4 \times 1$ PySCF)	0.560	0.429	0.557	0.401
m_{AFM} (\mathbf{k} - $4 \times 4 \times 1$ VASP)	0.592	0.350	0.591	0.327
m_{AFM} (\mathbf{k} - $4 \times 4 \times 2$ VASP)	0.590	0.350	0.590	0.334
m_{AFM} (\mathbf{k} - $6 \times 6 \times 4$ VASP)	0.591	0.358	0.590	0.327
Δn (in-plane)	-	-2.576	-	-2.698
Δn (out-of-plane)	-	-1.424	-	-1.302

3.5 Effect of geometry in Hg-1201

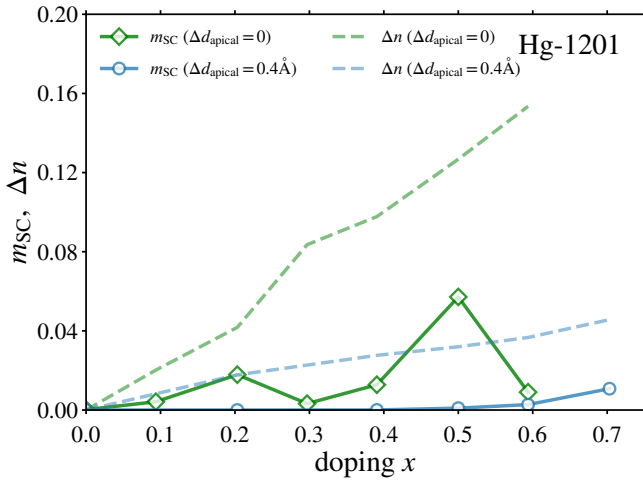


Figure S9: The scalar summed superconducting order m_{SC} and doped charges Δn on Cu after shifting the apical oxygen away from the CuO_2 plane of Hg-1201 (keeping the cell size the same). The shifted distances of apical oxygen are $\Delta d_{\text{apical}} = 0$ and 0.4 \AA .

The reduced and oxidized structures in Hg-1212 mainly differ by the length of the Cu-O bond, which leads to substantial differences in the effective doping of the Cu. To understand this better, we also investigated two structures of Hg-1201, where one has an artificially elongated apical Cu-O bond-length (keeping the other cell parameters fixed). In previous work on the parent state, we found that at the geometry with the elongated Cu-O bond, the effective J increases [22]. The descriptor trend in this work suggests then that the maximum pairing order should increase. However, on doping we find that the effective Cu doping decreases on this elongation of the Cu-O bond (similar to the difference between the Hg-1212 (red) and (ox) structures). This leads to a decrease in pairing order, despite the increase in J . The effect on J and on the effective Cu doping thus compete with each other as a function of apical oxygen distance, and this illustrates the subtlety of modeling apical oxygen effects, and the importance of an accurate charge distribution in the doped phases. We leave further investigations of this to future work.

3.6 Coupled-cluster amplitude decomposition data

Table S5: SVD decomposition of T_2 amplitudes. Singular values Σ and singular vector component (excitation) norms are shown.

spin-conserving				spin-fluctuating			
mode	Σ	excitation [multiplicity]	norm	Σ	excitation [multiplicity]	norm	
1	0.366			0.541			
		$\text{Cu } 3d_{x^2-y^2} \alpha \rightarrow \text{O } 2p_y \alpha [\times 2]$	0.023		$\text{Cu } 3d_{x^2-y^2} \alpha \rightarrow \text{Cu } 3d_{x^2-y^2} \beta [\times 4]$	0.074	
		$\text{Cu } 3d_{x^2-y^2} \beta \rightarrow \text{O } 2p_x \beta [\times 2]$	0.023		$\text{O } 2p_x \alpha \rightarrow \text{O } 2p_x \beta [\times 2]$	0.020	
		$\text{O } 2p_y \beta \rightarrow \text{Cu } 3d_{x^2-y^2} \beta [\times 2]$	0.008		$\text{O } 2p_y \alpha \rightarrow \text{O } 2p_x \beta [\times 4]$	0.008	
		$\text{O } 2p_x \alpha \rightarrow \text{Cu } 3d_{x^2-y^2} \alpha [\times 2]$	0.008		$\text{O } 2p_x \alpha \rightarrow \text{O } 2p_x \beta [\times 4]$	0.008	
		$\text{Cu } 3d_{yz} \beta \rightarrow \text{Cu } 4d_{yz} \beta [\times 2]$	0.007		
		$\text{Cu } 3d_{xz} \alpha \rightarrow \text{Cu } 4d_{xz} \alpha [\times 2]$	0.007				
					
2	0.362			0.453			
		$\text{Cu } 3d_{x^2-y^2} \alpha \rightarrow \text{O } 2p_y \alpha [\times 2]$	0.031		$\text{Cu } 3d_{x^2-y^2} \alpha \rightarrow \text{Cu } 3d_{x^2-y^2} \beta [\times 4]$	0.117	
		$\text{O } 2p_y \beta \rightarrow \text{Cu } 3d_{x^2-y^2} \beta [\times 2]$	0.020		$\text{O } 2p_x \alpha \rightarrow 10 \text{O } 2p_x \beta [\times 4]$	0.016	
		$\text{Cu } 3d_{x^2-y^2} \beta \rightarrow \text{O } 2p_x \beta [\times 2]$	0.015		$\text{O } 2p_y \alpha \rightarrow 10 \text{O } 2p_x \beta [\times 4]$	0.007	
		$\text{O } 2p_y \alpha \rightarrow \text{Cu } 3d_{x^2-y^2} \alpha [\times 2]$	0.013		$\text{O } 2p_x \beta \rightarrow 11 \text{O } 2p_y \beta [\times 2]$	0.006	
		$\text{Cu } 3d_{yz} \beta \rightarrow \text{Cu } 4d_{yz} \beta [\times 2]$	0.011		
		$\text{Cu } 3d_{xz} \beta \rightarrow \text{Cu } 4d_{xz} \beta [\times 2]$	0.011				
					
3	0.362			0.453			
		$\text{Cu } 3d_{x^2-y^2} \beta \rightarrow \text{O } 2p_x \beta [\times 2]$	0.031		$\text{Cu } 3d_{x^2-y^2} \alpha \rightarrow \text{Cu } 3d_{x^2-y^2} \beta [\times 4]$	0.073	
		$\text{O } 2p_x \alpha \rightarrow \text{Cu } 3d_{x^2-y^2} \alpha [\times 2]$	0.020		$\text{O } 2p_y \alpha \rightarrow 10 \text{O } 2p_x \beta [\times 4]$	0.021	
		$\text{Cu } 3d_{x^2-y^2} \alpha \rightarrow \text{O } 2p_y \alpha [\times 2]$	0.015		$\text{O } 2p_x \alpha \rightarrow 10 \text{O } 2p_x \beta [\times 4]$	0.013	
		$\text{O } 2p_x \beta \rightarrow \text{Cu } 3d_{x^2-y^2} \beta [\times 2]$	0.013		$\text{O } 2p_y \beta \rightarrow 10 \text{O } 2p_x \beta [\times 2]$	0.010	
		$\text{Cu } 3d_{xz} \alpha \rightarrow \text{Cu } 4d_{xz} \alpha [\times 2]$	0.011		
		$\text{Cu } 3d_{yz} \alpha \rightarrow \text{Cu } 4d_{yz} \alpha [\times 2]$	0.011				
					
4	0.361			0.344			
		$\text{Cu } 3d_{x^2-y^2} \beta \rightarrow \text{O } 2p_x \beta [\times 2]$	0.020	0	$\text{Cu } 3d_{x^2-y^2} \alpha \rightarrow 0 \text{Cu } 3d_{x^2-y^2} \beta [\times 4]$	0.074	
		$\text{Cu } 3d_{x^2-y^2} \alpha \rightarrow \text{O } 2p_y \alpha [\times 2]$	0.020		$8 \text{O } 2p_x \alpha \rightarrow 10 \text{O } 2p_x \beta [\times 2]$	0.020	
		$\text{O } 2p_y \alpha \rightarrow \text{Cu } 3d_{x^2-y^2} \alpha [\times 2]$	0.014		$4 \text{O } 2p_y \alpha \rightarrow 10 \text{O } 2p_x \beta [\times 4]$	0.008	
		$\text{O } 2p_x \beta \rightarrow \text{Cu } 3d_{x^2-y^2} \beta [\times 2]$	0.014		$5 \text{O } 2p_x \alpha \rightarrow 10 \text{O } 2p_x \beta [\times 4]$	0.008	
		$\text{O } 2p_y \beta \rightarrow \text{Cu } 3d_{x^2-y^2} \beta [\times 2]$	0.014		
		$\text{O } 2p_x \alpha \rightarrow \text{Cu } 3d_{x^2-y^2} \alpha [\times 2]$	0.014				
					
5	0.270			0.227			
		$\text{O } 2p_y \alpha \rightarrow \text{Cu } 3d_{x^2-y^2} \alpha [\times 2]$	0.009		$10 \text{O } 2p_x \alpha \rightarrow 10 \text{O } 2p_x \beta [\times 4]$	0.020	
		$\text{O } 2p_x \beta \rightarrow \text{Cu } 3d_{x^2-y^2} \beta [\times 2]$	0.009		$11 \text{O } 2p_y \alpha \rightarrow 10 \text{O } 2p_x \beta [\times 4]$	0.012	
		$\text{O } 2p_y \beta \rightarrow \text{Cu } 3d_{x^2-y^2} \beta [\times 2]$	0.009		$10 \text{O } 2p_x \alpha \rightarrow 3 \text{Cu } 4p_x \beta [\times 4]$	0.011	
		$\text{O } 2p_x \alpha \rightarrow \text{Cu } 3d_{x^2-y^2} \alpha [\times 2]$	0.009		$11 \text{O } 2p_y \alpha \rightarrow 11 \text{O } 2p_y \beta [\times 2]$	0.010	
		$\text{O } 2p_y \beta \rightarrow \text{O } 2p_y \beta [\times 2]$	0.006		
		$\text{O } 2p_x \alpha \rightarrow \text{O } 2p_x \alpha [\times 2]$	0.006				
					

4 Limitations of the current work

As discussed in the main text, the ab initio methodology developed in the current work reproduces the pressure effect and layer effect in a variety of cuprate materials and structures. Despite this agreement, it is important to note the omissions in the current treatment and areas where the methodology needs to be further improved in the future. These are summarized below.

The main limitations in the basic physics are:

1. Lack of long-range fluctuations. Because we are using a quantum impurity treatment, correlations are limited to being (mainly) across length-scales comparable to the impurity. (In DMET, the correlated fluctuations with the bath provide a limited treatment of longer range fluctuations outside of the impurity). This rules out pairing mechanisms which rely on long-range or even critical fluctuations. In principle, the pairing order we compute should be carefully converged with respect to the impurity size. This is possible in some cases for models [91] but will clearly be very challenging in a fully ab initio treatment.
2. Lack of explicit doping. As discussed in various places, the connection between chemical doping composition, and effective doping of the plane, is non-trivial and may not be adequately reproduced by the simple RBA and VCA treatments in this work. In addition, dopant atoms introduce disorder which may affect the ground-state order.
3. Lack of phonon degrees of freedom. Phonons are clearly of some importance in these materials, due to strong spin-phonon coupling.
4. Lack of temperature and spectra. Although the current formulation is a ground-state formulation, it is obviously important to include the effects of temperature, as well as to study dynamical effects.

There are also some technical limitations, which appear primarily due to the need to limit computational cost and to ensure numerical stability:

1. Dependence on the initial mean-field. Although the DMET impurity problem does not suffer from double-counting, the DMET self-consistency only modifies a small block of the lattice mean-field Hamiltonian, and elements outside of this block are thus tied to the original mean-field solution, here taken from PBE0. This may not be a good starting point. Indeed, if the charge density from PBE0 is poor we expect poor behaviour.
2. The convergence of DMET self-consistency and solvers. The convergence of the DMET self-consistent iteration (and to a lesser extent the many-body solver) is challenging in the doped regime where there are small gaps. The use of finite-temperature smearing here introduces a (small) inconsistency between the lattice treatment (at finite temperature) and the quantum impurity (where the many-body solver works at zero temperature).
3. Treatment of the chemical potential in the solver. Currently, the physical number of electrons is adjusted at the Hartree-Fock level in the quantum impurity for cost reasons, rather than at the correlated level.
4. Non-exactness of the approximate solvers. Although CCSD appears to be a good compromise between accuracy and speed, we may need more powerful solvers to study more exotic phases.
5. Basis set convergence. Although adequate for obtaining the trends in order parameters, the polarized double-zeta basis sets used are still small by the standards of chemical accuracy, where triple-zeta or larger basis sets are desirable.

5 Reference

- [1] N. Plakida, *High-temperature cuprate superconductors: Experiment, theory, and applications*, Vol. 166 (Springer Science & Business Media, 2010).
- [2] M. R. Norman, The challenge of unconventional superconductivity, *Science* **332**, 196 (2011).
- [3] L. Gao, Y. Xue, F. Chen, Q. Xiong, R. Meng, D. Ramirez, C. Chu, J. Eggert, and H. Mao, Superconductivity up to 164 K in $HgBa_2Ca_{m-1}Cu_mO_{2m+2+\delta}$ ($m = 1, 2$, and 3) under quasihydrostatic pressures, *Phys. Rev. B* **50**, 4260 (1994).
- [4] A. Yamamoto, N. Takeshita, C. Terakura, and Y. Tokura, High pressure effects revisited for the cuprate superconductor family with highest critical temperature, *Nat. comm.* **6**, 8990 (2015).
- [5] E. Antipov, A. Abakumov, and S. Putilin, Chemistry and structure of Hg-based superconducting Cu mixed oxides, *Supercond. Sci. Tech.* **15**, R31 (2002).
- [6] E. Dagotto, Complexity in strongly correlated electronic systems, *Science* **309**, 257 (2005).
- [7] L. N. d. Oliveira, E. Gross, and W. Kohn, Density-functional theory for superconductors, *Phys. Rev. Lett.* **60**, 2430 (1988).
- [8] M. Lüders, M. Marques, N. Lathiotakis, A. Floris, G. Profeta, L. Fast, A. Continenza, S. Massidda, and E. Gross, Ab initio theory of superconductivity. I. Density functional formalism and approximate functionals, *Phys. Rev. B* **72**, 024545 (2005).
- [9] M. Qin, T. Schäfer, S. Andergassen, P. Corboz, and E. Gull, The Hubbard model: A computational perspective, *Annu. Rev. Condens. Matter Phys.* **13**, 275 (2022).
- [10] M. T. Schmid, J.-B. Morée, Y. Yamaji, and M. Imada, Superconductivity studied by solving ab initio low-energy effective Hamiltonians for carrier doped $CaCuO_2$, $Bi_2Sr_2CuO_6$, $Bi_2Sr_2CaCu_2O_8$, and $HgBa_2CuO_4$, arXiv preprint arXiv:2303.06672 (2023).
- [11] B.-X. Zheng, C.-M. Chung, P. Corboz, G. Ehlers, M.-P. Qin, R. M. Noack, H. Shi, S. R. White, S. Zhang, and G. K.-L. Chan, Stripe order in the underdoped region of the two-dimensional Hubbard model, *Science* **358**, 1155 (2017).
- [12] E. W. Huang, C. B. Mendl, S. Liu, S. Johnston, H.-C. Jiang, B. Moritz, and T. P. Devereaux, Numerical evidence of fluctuating stripes in the normal state of high- T_c cuprate superconductors, *Science* **358**, 1161 (2017).
- [13] M. Qin, C.-M. Chung, H. Shi, E. Vitali, C. Hubig, U. Schollwöck, S. R. White, and S. Zhang, Absence of superconductivity in the pure two-dimensional Hubbard model, *Phys. Rev. X* **10**, 031016 (2020).
- [14] S. Jiang, D. J. Scalapino, and S. R. White, Ground-state phase diagram of the t - t' - J model, *Proc. Natl. Acad. Sci.* **118**, e2109978118 (2021).
- [15] P. Mai, N. S. Nichols, S. Karakuzu, F. Bao, A. Del Maestro, T. A. Maier, and S. Johnston, Robust charge-density-wave correlations in the electron-doped single-band Hubbard model, *Nat. Comm.* **14**, 2889 (2023).
- [16] P. R. C. Kent, T. Saha-Dasgupta, O. Jepsen, O. K. Andersen, A. Macridin, T. A. Maier, M. Jarrell, and T. C. Schulthess, Combined density functional and dynamical cluster quantum Monte Carlo calculations of the three-band Hubbard model for hole-doped cuprate superconductors, *Phys. Rev. B* **78**, 035132 (2008).
- [17] C. Weber, C. Yee, K. Haule, and G. Kotliar, Scaling of the transition temperature of hole-doped cuprate superconductors with the charge-transfer energy, *EPL* **100**, 37001 (2012).
- [18] N. Kowalski, S. S. Dash, P. Sémond, D. Sénéchal, and A.-M. Tremblay, Oxygen hole content, charge-transfer gap, covalency, and cuprate superconductivity, *Proc. Natl. Acad. Sci.* **118**, e2106476118 (2021).
- [19] X. Wang, L. De'Medici, H. Park, C. Marianetti, and A. J. Millis, Covalency, double-counting, and the metal-insulator phase diagram in transition metal oxides, *Phys. Rev. B* **86**, 195136 (2012).
- [20] J. Karp, A. Hampel, and A. J. Millis, Dependence of DFT+ DMFT results on the construction of the correlated orbitals, *Phys. Rev. B* **103**, 195101 (2021).
- [21] S. Jiang, D. J. Scalapino, and S. R. White, A single-band model with enhanced pairing from dmrg-based downfolding of the three-band hubbard model, arXiv preprint arXiv:2303.00756 (2023).
- [22] Z.-H. Cui, H. Zhai, X. Zhang, and G. K.-L. Chan, Systematic electronic structure in the cuprate parent state from quantum many-body simulations, *Science* **377**, 1192 (2022).
- [23] G. Knizia and G. K.-L. Chan, Density matrix embedding: A simple alternative to dynamical mean-field theory, *Phys. Rev. Lett.* **109**, 186404 (2012).
- [24] J. P. F. LeBlanc, A. E. Antipov, F. Becca, I. W. Bulik, G. K.-L. Chan, C.-M. Chung, Y. Deng, M. Ferrero, T. M. Henderson, C. A. Jiménez-Hoyos, E. Kozik, X.-W. Liu, A. J. Millis, N. V. Prokof'ev, M. Qin, G. E. Scuseria, H. Shi, B. V. Svistunov, L. F. Tocchio, I. S. Tupitsyn, S. R. White, S. Zhang, B.-X. Zheng, Z. Zhu, and E. Gull, Solutions of the two-dimensional Hubbard model: Benchmarks and results from a wide range of numerical algorithms, *Phys. Rev. X* **5**, 041041 (2015).
- [25] Z.-H. Cui, C. Sun, U. Ray, B.-X. Zheng, Q. Sun, and G. K.-L. Chan, Ground-state phase diagram of the three-band Hubbard model from density matrix embedding theory, *Phys. Rev. Research* **2**, 043259 (2020).
- [26] I. Shavitt and R. J. Bartlett, *Many-Body methods in chemistry and physics: MBPT and coupled cluster Theory* (Cambridge University, 2009).
- [27] G. K.-L. Chan and S. Sharma, The density matrix renormalization group in quantum chemistry, *Ann. Rev. Phys. Chem.* **62**, 465 (2011).

[28] J. W. Furness, Y. Zhang, C. Lane, I. G. Buda, B. Barbiellini, R. S. Markiewicz, A. Bansil, and J. Sun, An accurate first-principles treatment of doping-dependent electronic structure of high-temperature cuprate superconductors, *Comm. Phys.* **1**, 1 (2018).

[29] L. Bellaiche and D. Vanderbilt, Virtual crystal approximation revisited: Application to dielectric and piezoelectric properties of perovskites, *Phys. Rev. B* **61**, 7877 (2000).

[30] Y. Nambu, Quasi-particles and gauge invariance in the theory of superconductivity, *Phys. Rev.* **117**, 648 (1960).

[31] See supplementary materials.

[32] M. Azuma, Z. Hiroi, M. Takano, Y. Bando, and Y. Takeda, Superconductivity at 110 K in the infinite-layer compound $(\text{Sr}_{1-x}\text{Ca}_x)_{1-y}\text{CuO}_2$, *Nature* **356**, 775 (1992).

[33] F. Hardy, N. Hillier, C. Meingast, D. Colson, Y. Li, N. Barišić, G. Yu, X. Zhao, M. Greven, and J. Schilling, Enhancement of the critical temperature of $\text{HgBa}_2\text{CuO}_{4+\delta}$ by applying uniaxial and hydrostatic pressure: implications for a universal trend in cuprate superconductors, *Phys. Rev. Lett.* **105**, 167002 (2010).

[34] Q. Huang, J. Lynn, Q. Xiong, and C. Chu, Oxygen dependence of the crystal structure of $\text{HgBa}_2\text{CuO}_{4+\delta}$ and its relation to superconductivity, *Phys. Rev. B* **52**, 462 (1995).

[35] P. Radaelli, J. Wagner, B. Hunter, M. Beno, G. Knapp, J. Jorgensen, and D. Hinks, Structure, doping and superconductivity in $\text{HgBa}_2\text{CaCu}_2\text{O}_{6+\delta}$ ($T_c \leq 128$ K), *Physica C: Supercond.* **216**, 29 (1993).

[36] B. Lorenz and C. Chu, High pressure effects on superconductivity (Springer, 2005) pp. 459–497.

[37] J. S. Schilling, High-pressure effects, *Handbook of High-Temperature Superconductivity: Theory and Experiment*, 427 (2007).

[38] R. Liang, D. Bonn, and W. Hardy, Evaluation of cuO_2 plane hole doping in $\text{YBa}_2\text{Cu}_3\text{O}_{6+x}$ single crystals, *Phys. Rev. B* **73**, 180505 (2006).

[39] A. Yamamoto, W.-Z. Hu, and S. Tajima, Thermoelectric power and resistivity of $\text{HgBa}_2\text{CuO}_{4+\delta}$ over a wide doping range, *Phys. Rev. B* **63**, 024504 (2000).

[40] B.-X. Zheng and G. K.-L. Chan, Ground-state phase diagram of the square lattice Hubbard model from density matrix embedding theory, *Phys. Rev. B* **93**, 035126 (2016).

[41] L. Wang, G. He, Z. Yang, M. Garcia-Fernandez, A. Nag, K. Zhou, M. Minola, M. L. Tacon, B. Keimer, Y. Peng, and Y. Li, Paramagnons and high-temperature superconductivity in a model family of cuprates, *Nat. Comm.* **13**, 3163 (2022).

[42] P. W. Anderson, The resonating valence bond state in La_2CuO_4 and superconductivity, *Science* **235**, 1196 (1987).

[43] F. C. Zhang and T. M. Rice, Effective Hamiltonian for the superconducting Cu oxides, *Phys. Rev. B* **37**, 3759 (1988).

[44] S. M. O’Mahony, W. Ren, W. Chen, Y. X. Chong, X. Liu, H. Eisaki, S.-i. Uchida, M. Hamidian, and J. S. Davis, On the electron pairing mechanism of copper-oxide high temperature superconductivity, *Proc. Natl. Acad. Sci.* **119**, e2207449119 (2022).

[45] C. Weber, K. Haule, and G. Kotliar, Strength of correlations in electron-and hole-doped cuprates, *Nat. Phys.* **6**, 574 (2010).

[46] M. Jurkutat, C. Kattinger, S. Tsankov, R. Reznicek, A. Erb, and J. Haase, How pressure enhances the critical temperature of superconductivity in $\text{YBa}_2\text{Cu}_3\text{O}_{6+y}$, *Proc. Natl. Acad. Sci.* **120**, e2215458120 (2023).

[47] E. Pavarini, I. Dasgupta, T. Saha-Dasgupta, O. Jepsen, and O. Andersen, Band-structure trend in hole-doped cuprates and correlation with $T_{c\max}$, *Phys. Rev. Lett.* **87**, 047003 (2001).

[48] X. Dong, L. Del Re, A. Toschi, and E. Gull, Mechanism of superconductivity in the hubbard model at intermediate interaction strength, *Proc. Natl. Acad. Sci.* **119**, e2205048119 (2022).

[49] N. A. Bogdanov, G. Li Manni, S. Sharma, O. Gunnarsson, and A. Alavi, Enhancement of superexchange due to synergetic breathing and hopping in corner-sharing cuprates, *Nat. Phys.* **18**, 190 (2022).

[50] Z.-H. Cui, T. Zhu, and G. K.-L. Chan, Efficient implementation of ab initio quantum embedding in periodic systems: Density matrix embedding theory, *J. Chem. Theory Comput.* **16**, 119 (2020).

[51] N. Bogoliubov, V. V. Tolmachev, and D. Širkov, A new method in the theory of superconductivity, *Fortschritte der physik* **6**, 605 (1958).

[52] J.-P. Blaizot and G. Ripka, *Quantum theory of finite systems*, Vol. 3 (MIT press Cambridge, MA, 1986).

[53] P. W. Anderson, Random-phase approximation in the theory of superconductivity, *Phys. Rev.* **112**, 1900 (1958).

[54] L. Lin and X. Wu, Numerical solution of large scale Hartree-Fock-Bogoliubov equations, *ESAIM: Math. Model. Numer. Anal.* **55**, 763 (2021).

[55] J.-X. Zhu, *Bogoliubov-de Gennes method and its applications*, Vol. 924 (Springer, 2016).

[56] G. Knizia, Intrinsic atomic orbitals: An unbiased bridge between quantum theory and chemical concepts, *J. Chem. Theory Comput.* **9**, 4834 (2013).

[57] J. R. Bartlett and M. Musiał, Coupled-cluster theory in quantum chemistry, *Rev. Mod. Phys.* **79**, 291 (2007).

[58] P. Pulay, Convergence acceleration of iterative sequences. the case of SCF iteration, *Chem. Phys. Lett.* **73**, 393 (1980).

[59] C. Yang, J. Brabec, L. Veis, D. B. Williams-Young, and K. Kowalski, Solving coupled cluster equations by the Newton Krylov method, *Front. Chem.* **8**, 590184 (2020).

[60] D. A. Knoll and D. E. Keyes, Jacobian-free Newton-Krylov methods: a survey of approaches and applications, *J. Comput. Phys.* **193**, 357 (2004).

[61] MPI4PySCF, An MPI plugin for PySCF, <https://github.com/zhcui/mpi4pyscf>.

[62] T. Kinoshita, O. Hino, and R. J. Bartlett, Coupled-cluster method tailored by configuration interaction, *J. Chem. Phys.* **123**, 074106 (2005).

[63] S. R. White, Density matrix formulation for quantum renormalization groups, *Phys. Rev. Lett.* **69**, 2863 (1992).

[64] G. K.-L. Chan and M. Head-Gordon, Highly correlated calculations with a polynomial cost algorithm: A study of the density matrix renormalization group, *J. Chem. Phys.* **116**, 4462 (2002).

[65] U. Schollwöck, The density-matrix renormalization group in the age of matrix product states, *Ann. phys.* **326**, 96 (2011).

[66] G. K. Chan, A. Keselman, N. Nakatani, Z. Li, and S. R. White, Matrix product operators, matrix product states, and ab initio density matrix renormalization group algorithms, *J. Chem. Phys.* **145** (2016).

[67] S. Wouters, C. A. Jiménez-Hoyos, Q. Sun, and G. K.-L. Chan, A practical guide to density matrix embedding theory in quantum chemistry, *J. Chem. Theory Comput.* **12**, 2706 (2016).

[68] I. Mayer, Charge, bond order and valence in the ab initio SCF theory, *Chem. Phys. Lett.* **97**, 270 (1983).

[69] A. Damle, L. Lin, and L. Ying, Compressed representation of kohn–sham orbitals via selected columns of the density matrix, *J. Chem. Theory Comput.* **11**, 1463 (2015).

[70] L. Nordheim, The electron theory of metals, *Ann. Phys.* **9**, 607 (1931).

[71] S. Goedecker, M. Teter, and J. Hutter, Separable dual-space gaussian pseudopotentials, *Phys. Rev. B* **54**, 1703 (1996).

[72] C. Hartwigsen, S. Goedecker, and J. Hutter, Relativistic separable dual-space gaussian pseudopotentials from H to Rn, *Phys. Rev. B* **58**, 3641 (1998).

[73] J. Hutter, New optimization of GTH pseudopotentials for PBE, SCAN, PBE0 functionals. GTH pseudopotentials for Hartree-Fock. NLCC pseudopotentials for PBE, <https://github.com/juerghutter/GTH> (2019).

[74] H.-Z. Ye and T. C. Berkelbach, Correlation-consistent gaussian basis sets for solids made simple, *J. Chem. Theory Comput.* **18**, 1595 (2022).

[75] P.-O. Widmark, P.-Å. Malmqvist, and B. O. Roos, Density matrix averaged atomic natural orbital (ANO) basis sets for correlated molecular wave functions, *Theo. Chem. Acc.* **77**, 291 (1990).

[76] F. D. Murnaghan, The compressibility of media under extreme pressures, *Proc. Natl. Acad. Sci. U S A* **30**, 244 (1944).

[77] F. Birch, Finite elastic strain of cubic crystals, *Phys. Rev.* **71**, 809 (1947).

[78] Q. Sun, T. C. Berkelbach, N. S. Blunt, G. H. Booth, S. Guo, Z. Li, J. Liu, J. D. McClain, E. R. Sayfutyarova, S. Sharma, S. Wouters, and G. K.-L. Chan, PySCF: the Python-based simulations of chemistry framework, *WIREs Comput. Mol. Sci.* **8**, e1340 (2018).

[79] Q. Sun, X. Zhang, S. Banerjee, P. Bao, M. Barbry, N. S. Blunt, N. A. Bogdanov, G. H. Booth, J. Chen, Z.-H. Cui, J. J. Eriksen, Y. Gao, S. Guo, J. Hermann, M. R. Hermes, K. Koh, P. Koval, S. Lehtola, Z. Li, J. Liu, N. Mardirossian, J. D. McClain, M. Motta, B. Mussard, H. Q. Pham, A. Pulkin, W. Purwanto, P. J. Robinson, E. Ronca, E. Sayfutyarova, M. Scheurer, H. F. Schurkus, J. E. T. Smith, C. Sun, S.-N. Sun, S. Upadhyay, L. K. Wagner, X. Wang, A. White, J. D. Whitfield, M. J. Williamson, S. Wouters, J. Yang, J. M. Yu, T. Zhu, T. C. Berkelbach, S. Sharma, A. Sokolov, and G. K.-L. Chan, Recent developments in the PySCF program package, *J. Chem. Phys.* **153**, 024109 (2020).

[80] G. Kresse and J. Hafner, Ab initio molecular dynamics for liquid metals, *Phys. Rev. B* **47**, 558 (1993).

[81] G. Kresse and J. Hafner, Ab initio molecular-dynamics simulation of the liquid-metal–amorphous–semiconductor transition in germanium, *Phys. Rev. B* **49**, 14251 (1994).

[82] G. Kresse and J. Furthmüller, Efficiency of ab-initio total energy calculations for metals and semiconductors using a plane-wave basis set, *Comp. Mater. Sci.* **6**, 15 (1996).

[83] G. Kresse and J. Furthmüller, Efficient iterative schemes for *ab initio* total-energy calculations using a plane-wave basis set, *Phys. Rev. B* **54**, 11169 (1996).

[84] G. Kresse and D. Joubert, From ultrasoft pseudopotentials to the projector augmented-wave method, *Phys. Rev. B* **59**, 1758 (1999).

[85] P. E. Blöchl, Projector augmented-wave method, *Phys. Rev. B* **50**, 17953 (1994).

[86] J. P. Perdew, M. Ernzerhof, and K. Burke, Rationale for mixing exact exchange with density functional approximations, *J. Chem. Phys.* **105**, 9982 (1996).

[87] libDMET: A library of density matrix embedding theory (DMET) for lattice models and realistic solids, https://github.com/gkclab/libdmet_preview.

[88] H. Zhai and G. K.-L. Chan, Low communication high performance ab initio density matrix renormalization group algorithms, *J. Chem. Phys.* **154**, 224116 (2021).

[89] T. Zhu and G. K.-L. Chan, Ab initio full cell $GW +$ DMFT for correlated materials, *Phys. Rev. X* **11**, 021006 (2021).

[90] Y. Gao, Q. Sun, M. Y. Jason, M. Motta, J. McClain, A. F. White, A. J. Minnich, and G. K.-L. Chan, Electronic structure of bulk manganese oxide and nickel oxide from coupled cluster theory, *Phys. Rev. B* **101**, 165138 (2020).

[91] B.-X. Zheng, J. S. Kretchmer, H. Shi, S. Zhang, and G. K.-L. Chan, Cluster size convergence of the density matrix embedding theory and its dynamical cluster formulation: A study with an auxiliary-field quantum Monte Carlo solver, *Phys. Rev. B* **95**, 045103 (2017).